POLITECNICO DI MILANO
School of Industrial and Information Engineering

Master of Science in Nuclear Engineering

Reconstruction and Energy Extrapolation of the Implosion Core for Low-Converging Cryogenic Implosions

Advisor:
Prof. Matteo Passoni

Co-advisor:
Prof. Riccardo Betti
Co-advisor:
Dr. Arijit Bose

Graduation Thesis of:
Nicolas G. Luciani
863015

Academic Year 2016-2017

Abstract

The current thesis work was done in the context of inertial confinement fusion (ICF). In this approach to nuclear fusion energy research, the goal is to implode a target in order to heat its center to millions of degrees to produce enough fusion reactions to initiate a thermonuclear instability and obtain more fusion energy than is put into the system. Controlled nuclear fusion fullfilling these energy criteria has yet to be achieved in laboratory setting.

The two facilities currently pursuing ICF research in the U.S.A. rely on two different approaches: the National Ignition Facility (NIF) mainly focuses on indirect drive, while the OMEGA laser pursues spherically-symmetric direct drive. Since the NIF laser beams cannot currently be reconfigured to produce a spherically-symmetric direct illumination, the smaller scale implosions at OMEGA and used as a surrogate to test the direct drive approach.

It is the goal of this thesis project to provide extrapolations for high-adiabat, low-converging cryogenic OMEGA implosions to NIF energies of 1.9 to 2.5 MJ, in order to motivate NIF to pursue direct illumination in the future. Currently, it is estimated that fusion energy outputs of the order of ~ 5 times the current highest energy output obtained on NIF for the 1.9 MJ case and of the order of ~ 8 times in the 2.5 MJ case can be obtained on NIF with spherically-symmetric direct illumination. This work is mainly computational and relies on the reconstructon of implosion experiments performed on the OMEGA laser and a subsequent energy scaling to NIF energies using the theory of hydro-equivalent scaling, thus providing estimates for the main experimental observables. The computational tools used for this analysis are a 1-D implosion code for the acceleration phase of the implosion and a 2-D radiation hydrodynamics code used to simulate the deceleration phase of implosions. It should be pointed out that the reconstructions found for the purposes of this work may not be unique, but provide a close match with the experimental observables.

Sommario

Il presente lavoro di tesi si colloca nel contesto di ricerca di fusione a confinamento inerziale (ICF). In questo approccio, lo scopo è di far implodere un bersaglio in modo da scaldarne il centro a temperature di milioni di gradi , con lo scopo di ottenere un sufficiente numero di reazioni di fusione nucleare, causando un'instabilità termonucleare che permetta di ottenere più energia di quella introdotta nel sistema. Esperimenti di fusione che rispettino i criteri menzionati non sono mai stati effettuati in laboratorio.

Le due strutture prinicipali nell'ambito di ricerca ICF negli Stati Uniti sfruttano due approcci differenti: la National Ignition Facility (NIF) si concentra prevalentemente in approccio indiretto, mentre il laser OMEGA conduce esperimenti in approccio diretto a simmetria sferica. NIF correntemente non può essere configurato in modo da ottenere illuminazione diretta a simmetria sferica; di conseguenza, le implosioni su una scala minore effettuate su OMEGA sono utilizzate come surrogato per testare l'approccio diretto.

Lo scopo della presente tesi consiste nel fornire estrapolazioni idroequivalenti per implosioni con alto adiabat e bassa convergenza effettuate su OMEGA, sulla scala di NIF, ovvero a energie laser tra 1.9 e 2.5 MJ. I valori stimati per l'energia prodotta sulla scala di NIF con configurazione diretta a simmetria sferica sono stati stimati essere tra 5 e 8 volte superiori ai valori migliori ottenuti su NIF ad oggi. Questo lavoro di natura computazionale consiste nella ricostruzione degli esperimenti di OMEGA, seguita da un riscalamento alle energie di NIF, usando la teoria di idro-equivalenza, fornendo così stime per le principali osservabili. Gli strumenti utilizzati per questa analisi consistono in un codice di implosione 1-D per la fase di accelerazione e in un codice di fluidodinamica radiativa 2-D, utilizzato per simulare la fase di decelerazione. È necessario sottolineare che è possibile che le ricostruzioni trovate in questo lavoro di tesi non siano uniche, ma permettono di avere un buon accordo con i valori sperimentali.

Estratto

La principale risorsa energetica utilizzata nel presente contesto mondiale consiste in combustibili fossili. Il principale difetto dei combustibili fossili consiste nel fatto che sono la maggior fonte antropogenica di gas serra. Esistono tecnologie che permettono di produrre energia senza l'emissione delle ingenti quantità di gas serra, ma sono correntemente ostacolate da diversi fattori; i pannelli solari e l'eolico sono fonti di energia scostanti, correntemente inadatte a sostituire il carico di base in ogni momento della giornata o in ogni periodo nell'anno e la tecnologia per la conservazione dell'energia prodotta in eccesso alla domanda non è ancora sviluppata in maniera sufficiente da essere un'opzione. L'idroelettrico e il geotermico producono quantita' minime di gas serra ma centrali di quel tipo possono essere costruite solo in specifiche posizioni geografiche. La fissione nucleare e' una fonte di energia pulita in termini di emissioni di gas serra, ma è correntemente ostacolata dall'opinione pubblica a causa della complessità dei principi su cui si basa e delle tematiche ad essa legata.

La fusione nucleare offre una fonte di energia pulita e virtualmente inesauribile. È un processo che consiste nel far avvicinare due nuclei (carichi positivamente) a distanze simili al raggio d'azione della forza nucleare forte (10^{-15}m) in modo che possano unirsi in un singolo nucleo con un'energia di legame per nucleone superiore a quella dei due nuclei di partenza, rilasciando energia. Quest'energia può essere rilasciata sotto forma di radiazione elettromagnetica o come energia cinetica delle particelle risultanti. Quando un nucleo è incidente su un altro nucleo, vede una barriera dovuta al potenziale repulsivo Coulombiano. Questa barriera, a distanze dell'ordine del raggio d'azione della forza nucleare forte, dell'ordine di $10^{-15}m$, ha un'altezza $\approx 1.44 Z_1 Z_2$ eV. A distanze minori il potenziale attrattivo nucleare, in prima approssimazione uguale a una buca di potenziale, è predominante, e il contributo della repulsione Coulombiana diventa trascurabile. Di conseguenza

se un nucleo è in grado di superare la barriera, diventa possibile la fusione nucleare. Classicamente questo significa che affinchè possa avvenire la reazione sono necessarie energie dell'ordine di $1.44 Z_1 Z_2$ MeV; il tunneling quantistico però rende possibile la reazione anche a energie molto minori. Il combustibile più considerato è una miscela di Deuterio (D) e Trizio (T), due isotopi dell'idrogeno, che reagiscono secondo:

$$\mathrm{D} + \mathrm{T} \longrightarrow {}^{4}_{2}\mathrm{He} + \mathrm{n} + 17.6\,\mathrm{MeV} \tag{1}$$

I motivi per cui la scelta di combustibile spesso ricade su miscele di DT sono molteplici; tra questi, è una delle reazioni che rilascia più energia, ha le più alte probabilità di avvenire e genera un singolo neutrone per reazione, il che rende facilmente misurabile il numero di reazioni avvenute. Grazie al tunneling e ad altri aspetti legati alla fisica nucleare la reazione tra D e T ha la massima probabilità di avvenire a energie della particella incidente di 64 keV, molto minore dell'energia necessaria a superare classicamente la barriera Coulombiana.

Nonostante il fatto che la fusione sia stata teorizzata quasi 100 anni fa e che le reazioni utilizzate siano note da diversi decenni, il problema ignegneristico di riprodurre sulla terra, in condizioni sicure, un processo che avviene principalmente al centro delle stelle si è rivelato uno dei più complessi che l'umanità abbia mai affrontato, ed è tuttora senza soluzione. Nello spazio la fusione può avvenire perchè è possibile la formazione di oggetti con masse dell'ordine di 10^{29} e 10^{32} kg; su oggetti con simili masse, di vari ordini di grandezza superiori alla massa della terra stessa, la forza di gravità è sufficiente per confinare e riscaldare la materia più interna a temperature maggiori di 10^6 K. Di conseguenza i nuclei in questa regione hanno energie cinetiche sufficienti per superare la barriera coulombiana e fondersi con altri nuclei. Sulla terra, sono necessariamente stati sviluppati metodi diversi dal confinamento gravitazionale per confinare e riscaldare in maniera sufficiente i nuclei e permettere reazioni di fusione. Ognuno di questi metodi, che sotto molti punti di vista producono energia in maniera più efficiente del sole, è però affetto da svariate e complesse problematiche di natura ingegneristica, spesso differenti per i vari approcci. Tra questi, l'unico che è di provata efficacia è il confinamento inerziale (ICF, per Inertial Confinement Fusion), contesto all'interno del quale si colloca il presente lavoro di tesi.

La fusione tramite confinamento inerziale richiede un driver che possa comprimere un bersaglio, solitamente costituito da uno strato solido esterno (shell) contenente gas, in maniera sufficiente da innescare reazioni di fusione; queste a loro volta riscaldano ulteriormente il bersaglio, causando ulteriori reazioni. Questo processo avviene fintanto che il bersaglio rimane sufficientemente compresso; l'inerzia della shell è tale da permettere l'avvenimento di reazioni di fusione per tempi che correntemente sono dell'ordine di frazioni di nanosecondo. Affinchè questo processo possa essere considerato per la produzione di energia è necessario che non produca quantità eccessive di energia con una singola implosione, in modo da non danneggiare il contenimento del bersaglio, e che sia ripetibile a frequenze sufficientemente alte. Il driver e il combustibile correntemente più utilizzati sono i laser e miscele di DT. Il lavoro di tesi condotto dal candidato è stato effettuato al Laboratory for Laser Energetics (LLE) di Rochester, NY negli Stati Uniti. Questo laboratorio è una "User Facility" associata con l'università di Rochester. Questo significa che è prevista la possibilità per enti o organizzazioni esterne al laboratorio e all'università di utilizzare il laboratorio e il suo equipaggiamento. LLE è equipaggiato con un laser in grado di produrre 30 kJ di energia (dopo la conversione da IR a UV), che prende il nome di Omega, in configurazione "direct drive". Questo significa che il laser interagisce direttamente con il bersaglio; questo approccio è differente da quello di "indirect drive" utilizzato dalla National Ignition Facility, l'altro maggiore centro di ricerca ICF negli U.S.A., dove il laser colpisce un contenitore (hohlraum), contenente il bersaglio in modo da generare uno spettro molto simmetrico di raggi x, che a loro volta colpiscono il bersaglio. Entrambi gli approcci hanno pro e contro; a parità di energia laser, l'approccio diretto cede più energia al bersaglio, ma è fortemente affetto da instabilità laser plasma (LPI per laser plasma instabilities) e asimmetrie, mentre l'approccio indiretto è più simmetrico ed è meno affetto da LPI, ma cede meno energia al bersaglio.

Correntemente, il laser NIF non è equipaggiato per effettuare esperimenti di ICF diretta in configurazione sfericamente simmetrica; al laser mancano raggi nella regione equatoriale. Nonostante vengano effettuati esperimenti in configurazione "polar direct drive", questa configurazione non è ottimale e di conseguenza non è possibile ottenere una stima completa della performance di un'implosione diretta sfericamente simmetrica su quella scala. In aggiunta, spari su NIF richiedono cifre dell'ordine di milioni di dollari, mentre su Omega le cifre sono di quasi due ordini di grandezza minori. Da queste considerazioni nasce il presente lavoro di tesi.

Lo scopo di questa tesi è di ottenere stime della resa di neutroni e altre grandezze per ipotetiche implosioni basate su due delle implosioni migliori effettuate su Omega ri-scalate sulla scala di NIF. Con ri-scalamento, o meglio, ri-scalamento idrodinamicamente equivalente, si presuppone che un'implosione effettuata con un laser con energia minore venga ripetuta con un laser con energia maggiore in modo da mantenere la stessa densità di energia (i.e. pressione) in una regione centrale circondata da una shell con la stessa densità e forma, ma su un volume più grande. Per raggiungere questo scopo, è necessario avere, per Omega, delle simulazioni che riproducano i valori ottenuti con gli esperimenti. Questo non è banale in quanto le simulazioni con il codice 1-D (a simmetria sferica) LILAC producono risultati incredibilmente ottimistici, se confrontati con i risultati sperimentali. Il codice LILAC è un codice che modella completamente un'implosione, in 1-D. Date le condizioni iniziali e la forma dell'impulso laser simula l'implosione. Le discrepanze tra previsioni 1-D ed esperimento possone essere causate da diversi fattori. Tra questi, è possibile che il codice 1-D non modelli accuratamente l'implosione, o che siano presenti meccanismi che rendono l'implosione un fenomeno non a simmetria sferica, richiedendo simulazioni 2 o 3 dimensionali.

La vasta differenza tra le principali variabili utilizzate per determinare la qualità di una data implosione e i valori sperimentali suggerisce che la modellazione 1-D sia troppo ottimistica. Di conseguenza sono stati testati diversi meccanismi ad-hoc di degradazione dell'implosione, basati su modifiche del profilo dell'impulso laser, in modo da causare degradazioni 1-D rispetto alla simulazione originale. È quindi stato effettuato uno studio sistematico dei risultati di questi meccanismi di degradazione in modo da determinare se fosse possibile ottenere i valori sperimentali da tali simulazioni. Per questo scopo, sono stati utilizzati grafici come quelli in fig. 1, che rappresentano le tendenze delle principali osservabili caratterizzanti le implosioni. È stato possibile trovare simulazioni con valori molto vicini a quelli sperimentali, soprattutto se confrontati con i valori previsti dalla simulazione 1-D originale.

In seguito, sono stati effettuati studi su possibili meccanismi di degradazione 2-D, a partire dalle simulazioni 1-D selezionate durante la prima fase di degradazione, utilizzando il codice di fluidodinamica radiativa DEC2D. Questo non è un codice di implosione completo, e di conseguenza viene solitamente utilizzato in aggiunta a LILAC; viene selezionato un istante, solitamente vicino alla fine dell'impulso laser, in cui iniziare la simulazione in DEC2D, dopodichè i profili delle varie grandezze idrodinamiche a quell'istante di tempo sono importati da LILAC a DEC2D. Solitamente DEC2D viene utilizzato per modellare la fase in cui la produzione di neutroni è significativa, in

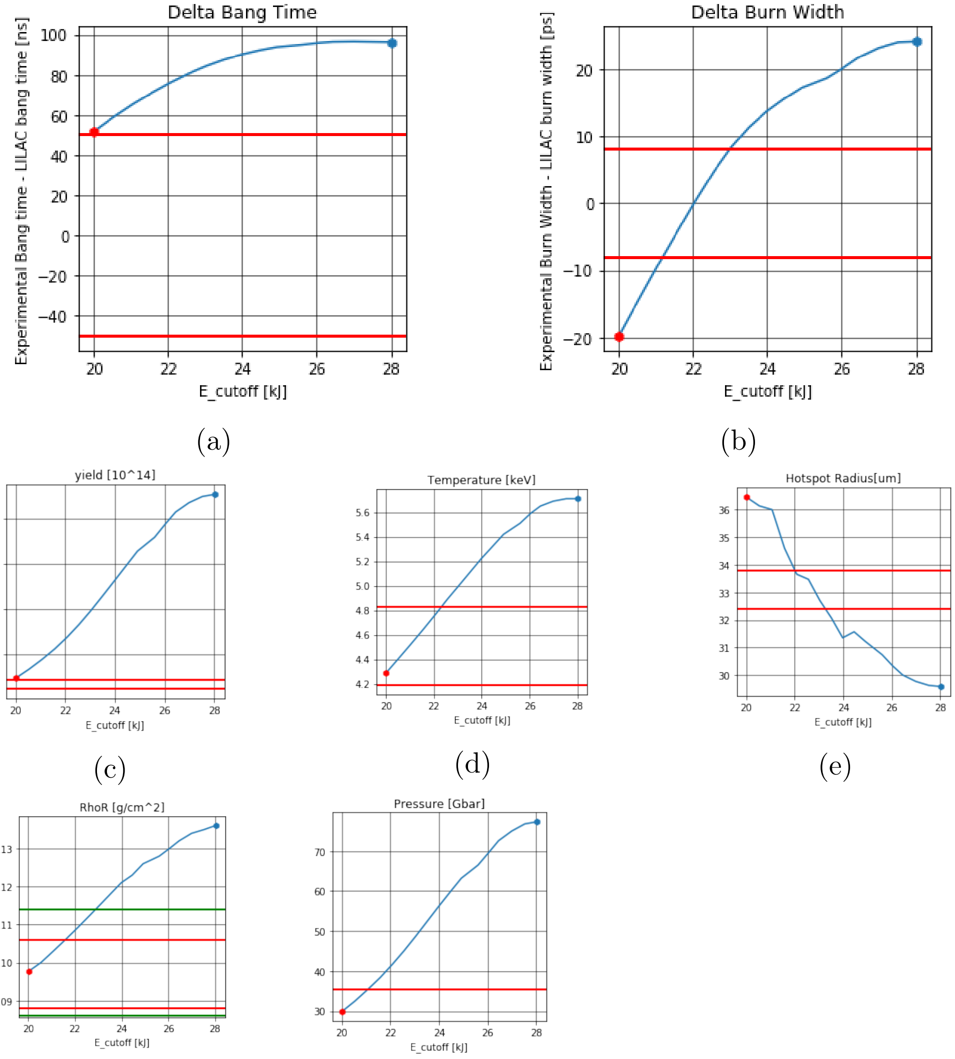

(a) (b)

(c) (d) (e)

(f) (g)

Figure 1: Risultati della degradazione 1-D derivante da uno dei meccanismi studiati nel contesto del presente lavoro di tesi.

Table 1: This table shows the experimental results (exp.), compared with the results from the original 1-D simulation (LILAC) and the best reconstruction found for the two shots analyzed (comp.), 87266 and 88314. Part I

Shot Number	**Temperatura Ionica** [keV]	**Raggio** [μm]	**Densità Areale**[mg/cm^2]
87266, Exp.	4.51 ± 0.32	33.1 ± 0.7	98.5 ± 11.5
87266, LILAC	5.71	27.22	136
87266, Comp.	4.04	30.0	99
88314, Exp.	4.32 ± 0.30	31.4	126.5 ± 14.5
88314, LILAC	5.79	24.04	183
88314, Comp.	4.52	25.3	143

Table 2: This table shows the experimental results (exp.), compared with the results from the original 1-D simulation (LILAC) and the best reconstruction found for the two shots analyzed (comp.), 87266 and 88314. Part II

Shot Number	**Resa di neutroni** [10^{14}]	**Pressione** [Gbar]	**Burn Width** [ps]	**Bang Time** [ns]
87266, Exp.	1.34 ± 0.1	35.5	81 ± 8	2.193 ± 0.05
87266, LILAC	5.53	95.0	57	2.097
87266, Comp.	1.34	43.5	87	2.151
88314, Exp.	1.28 ± 0.06	40.2	78 ± 8	2.155 ± 0.05
88314, LILAC	7.81	139.5	53	2.170
88314, Comp.	1.31	54.3	70	2.185

quanto la maggior parte delle osservabili sono valori integrali, pesati sull tasso di produzione di neutroni. In DEC2D, è prevista la possibilità di introdurre vari tipi di perturbazioni di diverse ampiezze. Questo tipo di degradazione ha un fondamento fisico: l'instabilità Rayleigh-Taylor amplifica le perturbazioni nel corso dell'implosione, quindi piccole asimmetrie causate dalla geometria dei raggi laser o da altri effetti possono propagarsi e crescere, diventando significative. Di conseguenza, nel contesto della presente tesi, sono stati introdotti diversi tipi di perturbazioni, in base al tipo di discrepanze rispetto ai dati sperimentali, e sono stati analizzati i risultati in modo da trovare le perturbazioni che forniscono il miglior accordo con i l'esperimento, anche se è necessario menzionare che i tipi di degradazione trovati possono non essere gli unici che riproducono i risultati sperimentali. I risultati, confrontati con i valori sperimentali e i valori della simulazione 1-D originale sono illustrati nelle tabelle 1 e 2

A seguito di queste ricostruzioni delle implosioni ottenute sperimentalmente, queste sono state ri-scalate in maniera idrodinamicamente equivalente, in modo da ottenere stime dei valori ottenibili su NIF in configurazione

diretta e sfericamente simmetrica. In questo modo è stato trovato che se fosse possibile riprodurre alcune delle implosioni effettuate su Omega su NIF, si otterrebbero energie tra cinque e nove volte superiori ai migliori valori ottenuti su NIF. Questo corrisponde a energie di fusione tra 250 e poco più di 450 kJ. Implosioni con tali rese richiederebbero ancora tempi e finanziamenti per raggiungere lo scopo di ottenere più energia di quella immessa nel sistema, ma sarebbero in grado di produrre frazioni significative dell'energia iniziale, possibilmente portando a un maggiore interesse verso le tematiche legate alla fusione e a maggiori finanziamenti.

Contents

Abstract **i**

Sommario **iii**

Estratto **v**

List of Figures **xiv**

List of Tables **xx**

1 Introduction **1**
- 1.1 Motivation 1
- 1.2 Thesis Outline 3

2 Inertial Confinement Fusion **5**
- 2.1 Introduction 5
- 2.2 Nuclear Fusion 6
- 2.3 Inertial Confinement Fusion 9
- 2.4 Basic Concepts in ICF Theory 14
- 2.5 Implosion and Instabilities 20

3 Trends in Experiments and Recontruction of the Implosion Core **25**
- 3.1 Introduction 25
- 3.2 Experimental results for 87266 and 88314 27
- 3.3 1-D Reconstruction of the Implosion Core 30
- 3.4 2-D Reconstruction of the Implosion Core 38
- 3.5 Final Comparison With Experiment 45

4 Hydrodynamically Equivalent Scaling of the Implosion Core 47
4.1 Introduction 47
4.2 Theory 49
4.3 Simulations 55
4.4 Conclusion 59

5 Conclusion and Further Work 63

Appendices 67

A Deceleration Phase Python Code 69

Bibliography 77

List of Figures

1 Risultati della degradazione 1-D derivante da uno dei meccanismi studiati nel contesto del presente lavoro di tesi. ix

2.1 Binding energy per nucleon plotted as a function of the mass number A. It is adapted from ref. [1] 7

2.2 Illustrations of the main phases in an ICF implosion. The cryogenic DT target is compressed to high densities via the use of X-rays or lasers. This compression heats the target, specifically the core, to very high density, initiating fusion reactions. The goal is to compress the target to sufficiently high densities and temperatures to initiate a burn wave of fusion reactions, burning through the cryogenic shell. This illustration is taken from ref. [7]. 10

2.3 Illustration of the Omega laser bay and target chamber (a) and a schematic illustration of the concept of direct drive ICF (b). This illustration is taken from ref. [7]. 11

2.4 Depiction of the concepts of low (a) and mid-mode (b) asymmetries. While it is believed that the main asymmetries on indirect-drive NIF are of the former type, a direct drive configuration would cause a combination of both. This illustration is taken from ref. [7]. 12

2.5 This illustration is taken from ref. [7]. 13

2.6 Schematic representation of the properties of a fluid on the two side of a shock front. 18

2.7 Schematic representation of laser pulse for an ICF implosion. t_{sb} stands for shock breakout time, and refers to the time required for the shock to reach the rear target surface. The laser pulse shown here is a typical configuration, consisting of a low intensity "foot", followed by a smooth increase to the full laser intensity, which is then maintained in order to further increase the convergence of the target, defined as the ratio of the initial shell radius and the size of the hotspot, leading to a "flat top". The intensities shown are typical intensities for ICF laser pulses. 19

2.8 Schematic view of a RT unstable system, i.e. a system for which $\nabla\rho \cdot \nabla P < 0$. The pedices "h" and "l" refer to "heavy" and "light" densities. The equilibrium pressure is given by $P_0(z) = Const. - \rho_0 g z$, with $\rho_0 = \rho_h$ for $z > 0$ and $\rho_0 = \rho_l$ for $z < 0$, and must be continuous at the interface. The image is adapted from ref. [7] 20

2.9 Perturbed interface between a heavy fluid with density ρ_h supported by a lighter fluid with density ρ_l(left). The perturbation has a wavelength = λ. On the right the profile of the density as a function of z is plotted, showing a characteristic scale length of L. The image is adapted from ref. [7] 23

2.10 Perturbed interface between a heavy fluid with density ρ_h supported by a lighter fluid with density ρ_l(left). The perturbation has a wavelength = λ; mass ablation causes the diffused density profile on the right, showing a characteristic scale length of L. Transitioning to the reference frame of the interface, the heavy fluid moves towards it with the ablation velocity v_a, crosses the interface, and blows off into the low density region with a higher velocity (v_b, blow-off velocity). The image is adapted from ref. [7] 23

3.1 Laser pulses and target dimensions for shots 87266 and 88314 29

3.2 Variation in the observables caused by modifications of the laser of type 1 for 87266, plotted as functions of E_{cutoff}; the first two plots, namely fig. 3.2a and 3.2b, are the curves for bang time deltas and burn width deltas. The following plots are, in order, the curves representing the degradations trends of yield, temperature, radii, areal densities, and lastly pressures. As previously stated, for degradations of type 1, the x axis corresponds to the values E_{cutoff}. Each point in the blue curves corresponds to observables from different LILAC simulations. The red points represent the values for the observables of the selected simulation, and the two red lines present in each plot give the range provided by the experimental measurement. It should be noted that for the case of the pressure, no straightforward error bars were available, therefore in figure 3.2g there is only one red line, the one corresponding to the inferred pressure. 32

3.3 Variation in the observables caused by modifications of the laser of type 2 for 87266, plotted as functions of P_{cutoff}; the first two plots, namely fig. 3.2a and 3.2b, are the curves for bang time deltas and burn width deltas. The following plots are, in order, the curves representing the degradations trends of yield, temperature, radii, areal densities, and lastly pressures. As previously stated, for degradations of type 2, the x axis corresponds to the values of P_{cutoff}. Each point in the blue curves corresponds to observables from different LILAC simulations. The black dashed lines correspond to the values of the observables for the selected simulation, and the two red lines present in each plot give the range provided by the experimental measurement. It should be noted that for the case of the pressure, no straightforward error bars were available, therefore in figure 3.3g there is only one red line, the one corresponding to the inferred pressure. 33

3.4 Variation in the observables caused by modifications of the laser of type 1 for 88314, plotted as functions of E_{cutoff}; the first two plots, namely fig. 3.4a and 3.4b, are the curves for bang time deltas and burn width deltas. The following plots are, in order, the curves representing the degradations trends of yield, temperature, radii, areal densities, and lastly pressures. As previously stated, for degradations of type 1, the x axis corresponds to the values of E_{cutoff}. Each point in the blue curves corresponds to observables from different LILAC simulations. The red points represent the values of the observables for the selected simulation, and the two red lines present in each plot give the range provided by the experimental measurement. It should be noted that for the case of the pressure, no straightforward error bars were available, therefore in figure 3.4g there is only one red line, the one corresponding to the inferred pressure. 35
3.5 Variation in the observables caused by modifications of the laser of type 2 for 87266, plotted as functions of E_{cutoff}; the first two plots, namely fig. 3.4a and 3.4b, are the curves for bang time deltas and burn width deltas. The following plots are, in order, the curves representing the degradations trends of yield, temperature, radii, areal densities, and lastly pressures. As previously stated, for degradations of type 2, the x axis corresponds to the values of E_{cutoff}. Each point in the blue curves corresponds to observables from different LILAC simulations. The black dashed lines correspond to the values of the observables for the selected simulation, and the two red lines present in each plot give the range provided by the experimental measurement. It should be noted that for the case of the pressure, no straightforward error bars were available, therefore in figure 3.5g there is only one red line, the one corresponding to the inferred pressure. 36
3.6 Trends caused by mode two degradations (in blue) and by mode 10(in orange) for 87266. YOC stand for "yield over clean", and is the ratio between the yield and the yield with no degradation. The red lines provide the range of acceptable values, and are based on the experimental measurements, plus or minus the error. 42

3.7 Trends caused by mode two degradations (in blue) and by a flat spectrum from mode 4 to 20 with a $1/l^2$ decay for modes higher than 20 (in orange) for 88314. YOC stand for "yield over clean", and is the ratio between the yield and the yield with no degradation. The red lines provide the ranges of acceptable values, and are based on the experimental measurements, plus or minus the error. The dots on the curves correspond to the final value selected for that type of perturbation. The third point is the point corresponding to the 2-D degraded simulation, with a combination of the two types of degradation. 44

4.1 Mass density profiles at bang time for shots 87266 and 88314, on both Omega and 1.9 MJ NIF scale. 60

List of Tables

1 This table shows the experimental results (exp.), compared with the results from the original 1-D simulation (LILAC) and the best reconstruction found for the two shots analyzed (comp.), 87266 and 88314. Part I x
2 This table shows the experimental results (exp.), compared with the results from the original 1-D simulation (LILAC) and the best reconstruction found for the two shots analyzed (comp.), 87266 and 88314. Part II x

3.1 This table shows the experimental results (exp.), compared with the results from the original 1-D simulation (LILAC) and the best reconstruction found for the two shots analyzed (comp.), 87266 and 88314. Part I 26
3.2 This table shows the experimental results (exp.), compared with the results from the original 1-D simulation (LILAC) and the best reconstruction found for the two shots analyzed (comp.), 87266 and 88314. The two value for the areal density correspond, in order, to MRS and ntof measurements. Part II 26
3.3 Experimental results with the corresponding clean LILAC simulation, part I 28
3.4 Experimental results with the corresponding clean LILAC simulation, part II 28
3.5 Comparison between the $E_{cutoff} = 20$ kJ simulations in LILAC and DEC2D for 87266 and 88314, part I. The experimental results are also present for convenience. Note that the radii from LILAC are not exactly the ones present in the plots in section 3.3, as the ones in this table have been calculated using SPECT3D. 40

3.6 Comparison between the $E_{cutoff} = 20$ kJ simulation in LILAC and DEC2D for 87266 and 88314, part II. The experimental results are also present for convenience. Note that the radii from LILAC are not exactly the ones present in the plots in section 3.3, as the ones in this table have been calculated using SPECT3D. 40

3.7 Comparison between the 20 kJ simulations in LILAC and DEC2D for 87266 and 88314, part I. The experimental results are also present to make the comparison easier. Note that the radii from LILAC are not exactly the ones present in the plots in section 3.3, as the ones in this table have been calculated using SPECT3D. Comp. stands for "computed" . . 46

3.8 Comparison between the 20 kJ simulation in LILAC and DEC2D, part II. The experimental results are also present to make the comparison easier. Note that the radii from LILAC are not exactly the ones present in the plots in section 3.3, as the ones in this table have been calculated using SPECT3D. 46

4.1 Observables for the cores reconstructed in chapter 3. Part I . . 54

4.2 Observables for the cores reconstructed in chapter 3. Part II . 54

4.3 Neutron yields and values of χ_{no_α}obtained from analytic calculations based on hydrodynamic equivalency, for different laser energies. 54

4.4 Neutron yields and values of $\hat{Y}_{amp}$ obtained from analytic calculations based on hydrodynamic equivalency, for different laser energies. 55

4.5 Neutron yields and values of χ_{no_α}obtained from numerical simulations relying on hydrodynamic equivalency, for different laser energies. The values for the χ_{no_α} in this case are obtained from the observables obtained in the "no-α"simulation, shown in table 4.7. 57

4.6 Neutron yields and values of $\hat{Y}_{amp}$ obtained from numerical simulations relying on hydrodynamic equivalency, for different laser energies. It should be noted that in this case, the yield amplification is inferred from the ratio $\frac{\text{yield with alpha deposition}}{\text{yield without alpha deposition}}$. 57

4.7 Results for the 1.9 MJ upscaling of 87266 and 88314 (with and without alpha burning) compared to the reconstructed Ω simulation. Theor. and num. respectively correspond to theoretical and numerical. 58

Chapter 1

Introduction

1.1 Motivation

The main driver for fusion research today is energy. The modern world in which we live needs a lot of energy. Mankind has reached a level of technological advancement inconceivable in the past. This technology allows us to live more comfortable lives, full of possibilities, services and commodities previously unimagined. We can travel anywhere in the world within hours, we have access to the world's knowledge through devices that can fit in our pockets, we can communicate instantly with people all over the world, and many other marvelous things.

Unfortunately all of this has come with a cost. These possibilities and technologies require massive amounts of energy. In today's world, the main energy source consists in fossil fuels. In 2015, according to the Organisation for Economic Co-operation and Development (OECD), fossil fuels were used to produce over 60 % of the electric energy required by the world. In addition to this, the world uses fossil fuels also for transportation, heat and more. The world's demand for fossil fuels since 1950 has increased more than six times and although there have been technological advancements leading to "cleaner" machines using fossil fuels, the world's greenhouse gas (GHG) emissions have increased by a similar factor; considering that it's currently believed that GHGs are the main contribution to climate change due to Mankind, these are very worrisome trends.

We have some alternative sources of energy, but they are currently not fit to fully substitute fossil fuels. Solar panels and wind turbines are unpredictable and therefore, with today's technology, are unfit to substitute the steady stream of energy provided by traditional fossil fuel plants; nuclear power is a carbon free alternative, but it seems to be facing a losing battle with public opinion, partially because of concerns about long term storage for nuclear waste, and partially on the grounds of the arguably incorrect opinion that nuclear power "isn't safe" (a 2013 Nasa study estimated that An average of 76,000 deaths per year were avoided annually between 2000-2009[thanks to the use of nuclear power][23]); hydropower and geothermal have a limited impact on the environment, but can only be built in specific locations.

There have been some positive signs in recent years, for instance there has been an increase in the use of renewable energies, but this growth has been very slow, and hasn't been sufficient to reduce the demand for fossil fuels. Nuclear fusion offers the cleanest alternative for completely substituting fossil fuels. The main fuel currently being studied for nuclear fusion is made up of two isotopes of hydrogen, which is an element that makes up more than 99% of the matter in the visible universe, and the byproducts of nuclear fusion reactions involving this type of fuel consist mainly in helium, which isn't toxic or harmful, unlike the byproducts of fossil fuels. Furthermore, a fusion reactor wouldn't suffer from the possibility of a meltdown. In addition to that, it could be used to render the nuclear waste from existing (or future) nuclear fission plants non-radioactive, thus solving the main controversial aspect of nuclear fission power plants. It has actually been estimated that a hybrid fusion-fission nuclear power plant could be used to increase the output of a regular fusion power plant, thus making the harnessing of fusion energy even closer.

There exists an additional driver for fusion energy research in countries possessing nuclear weapons. In the United States it takes the name of Stockpile Stewardship and Management program. This driver is the upkeep and maintenance of nuclear arsenals. Nuclear bombs are the deadliest weapons ever created by man. Otto Hahn's discovery of the fission of Uranium in 1938 set in motion a chain of events that would culminate on July 16th 1945 with the explosion of the first nuclear bomb in the world. Since then, even more powerful bombs were invented, but since they were first used in 1945, none of them have been used in conflict. As of 2016, all but three countries have even signed a treaty banning all nuclear explosions, for both civilian and military purposes. This is a symptom of a change of mentality regarding war, in light of the mutually assured destruction that has come with nuclear weapons. Nuclear weapons should not be seen as a cautionary tale for mankind's search for knowledge; the fact that there haven't been any conflicts on the scale of the World Wars since the second one ended in 1945 suggests they should be seen as a necessary step in a transition to a war free world. While further negotiations are indeed necessary to reach agreements to dismantle all nuclear arsenals, it is unsafe for any nuclear power to unilaterally decide to dismantle their own. Therefore, the upkeep of nuclear arsenals is necessary; research in inertial confinement fusion is one of the factors that has allowed the United States and other nuclear powers to maintain their weapons without the release of radioactive elements into the environment.

In addition to the two drivers mentioned above, fusion research is also advancing Mankind's undersanding of the physical world, and in particular of physics under extreme conditions, and has contributed to founding a new branch of physics, namely high energy density physics (HEDP). Thanks to fusion research, very diverse fields of science have progressed immensely: material science, lasers, and superconducting magnets, to name a few.

1.2 Thesis Outline

The final goal of this thesis to show that reproducing on NIF (National Ignition Facility) scale the best performing shots obtained on the Omega laser would yield up to roughly 8 times more energy than the best performing shot on NIF to date.

Chapter 2 introduces the reader to the field of inertial confinement fusion. Starting from the concept of nuclear fusion, all the main aspects related to ICF are illustrated and contextualized. The main facilities in the U.S.A. are introduced and some of their achievements are illustrated, followed by a section (2.4) aiming at providing the reader with all of the tools and modeling necessary to understand concepts in ICF. Lastly, a section on Rayleigh-Taylor instability is provided, and its connection to the work done in this thesis is explained.

After these introductory chapters, the main body of the thesis begins: the work done by the candidate at the laboratory for laser energetics. In 3 the experimental results from two of the best performing shots on Omega are shown and compared with the respective predictions of 1D simulations, in order to understand which degradation mechanisms are more likely to be at play. After this is done, it is shown in detail how using specific degradation mechanisms the experimental results can be reconstructed starting from simulations that heavily overestimated the implosion performance. Chapter 4 then provides the main results from the theory of hydro-equivalent scaling, in order to subsequently apply them to the implosion cores reconstructed in the previous chapter, both in an anlytical and in a numerical fashion; the results coming from the two are then analyzed and compared.

Finally, chapter 5 presents a summary of the work done and the possibilities for future works.

Chapter 2

Inertial Confinement Fusion

2.1 Introduction

This thesis work focuses on topics in inertial confinement fusion. Therefore it is neessary to provide the reader with an appropriate background on the subject. This is provided in the current chapter. In particular, in section 2.2 the topic of nuclear fusion is introduced. The necessary physical concepts are explained, and a very brief description of the two main approaches currently being pursued is then provided.

In section 2.3 the reader is introduced to ICF. The main ideas of ICF are illustrated, together with an overview of the main concepts that characterize ICF. The two facilities existing in the U.S.A. are described and compared, and the advantages and disadvantages of each are illustrated.

Subsequently, in section 2.4 a more detailed and theoretical description of ICF is provided. The main equations and characteristic quantities are introduced; some important formulae for obtaining estimates are also provided.

Lastly, in section 2.5, the Rayleigh-Taylor instability (RTI) is explained and a simple derivation of an important parameter, namely the linear growth rate, is provided. Additionally, it is the purpose of this section to illustrate the importance of RTI in ICF research and to provide a connection with the work done for the purposes of this thesis.

2.2 Nuclear Fusion

Mankind's mission to comprehend the composition of matter is a long and fascinating one. It is a quest that has infinitely enriched mankind's understanding of the physical universe and has seen contributions from some of the greatest human minds, of the caliber of Ernest Rutherford, Albert Einstein, and James Chadwick. It is impossible to provide a list of all the contributors but a taste of it can be found in ref. [31].

The last addition to the list of fundamental particles making up matter on earth and the periodic table of elements was the neutron, discovered in 1932. Since then, it is known that all atoms are made up of only three types of particles: electrons, protons and neutrons; of these the first two possess an electromagnetic charge (respectively, negative and positive) while the last is neutral. Neutrons and protons are bound by the strong nuclear force in an overall positively charged nucleus. This interaction is independent on the electromagnetic charge, and has the same intensity for both protons and neutrons. For this reason, the two are often referred to as nucleons. Around the nucleus is a negatively charged cloud of electrons.

As the name suggests, nuclear fusion refers to the possibility of uniting two nuclei into a single one. This has been considered a possibility ever since it was discovered in early 20^{th} century that the weight of a nucleus is measurably smaller than the particles that compose it. In light of Einstein's famous equation, $E = mc^2$, where E is the rest energy, m is the mass, and c is the speed of light, this allows for the possibility to fuse two nuclei into a single, more bounded one, lighter than the sum of its parts, releasing energy. The mass of the system would be thus reduced by a factor of Δm, providing an amount of energy equal to Δmc^2. A consequence of the fact that the system is tightly bound is that it requires an amount of energy of at least Δmc^2 to break it into its constituents. For this reason Δmc^2 takes the name of nuclear binding energy.

It is particularly useful to define the concept of nuclear binding energy per nucleon (B/A), equal to the binding energy of a given nucleus, divided by the mass number (which is given by sum of the number of protons and that of neutrons). The curve of the binding energy per nucleon is shown in 2.1. A quick look at this curve suggests two possible mechanisms for the production of energy, which take the names of fission and fusion. Both of them rely on the idea of moving from regions of the graph with lower binding energy towards more tightly bound nuclei, in order to release energy.

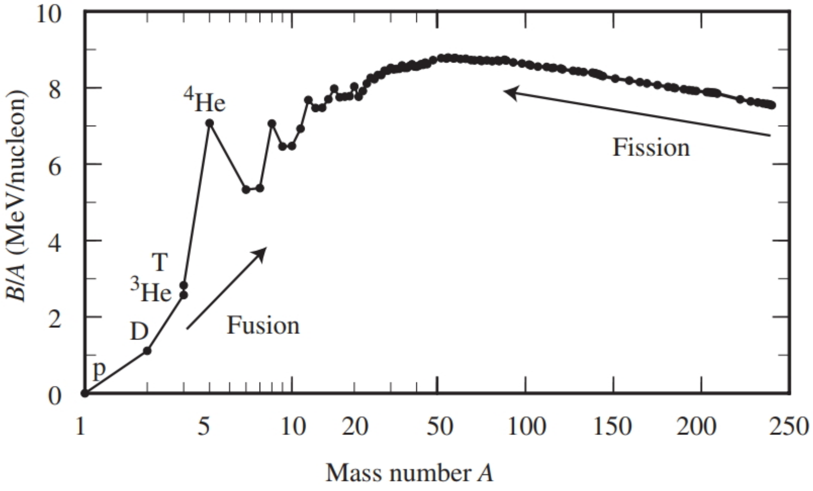

Figure 2.1: Binding energy per nucleon plotted as a function of the mass number A. It is adapted from ref. [1]

The former consists in splitting a heavy, more loosely bound nucleus into smaller, more tightly bound nuclei. For instance, this is done in many nuclear fission reactors by destabilizing an originally meta-stable Uranium-235 nucleus by causing it to absorb a neutron, leading it to split into smaller, more tightly bound nuclei. If the nucleus is sufficiently unstable, it may not even require an external agent to trigger this reaction. This is the case of nuclei such as Californium-252, which has a 7% probability of undergoing spontaneous fission. In a similar way, one can fuse more loosely bound light elements ($Z<28^{17}$,$A<56$) and obtain a single, more tightly bound nucleus, weighing less than the two nuclei reacting. This is the basis of nuclear fusion. Both reactions mentioned above can be written in the form

$$\mathrm{A} + \mathrm{B} \longrightarrow \mathrm{C} + \mathrm{D}, \tag{2.1}$$

where the number of elements on each side can vary. With this in mind, it is straightforward to calculate the released energy. It is given by:

$$E = \sum (\frac{B}{A})_i A_i - \sum (\frac{B}{A})_f A_f, \tag{2.2}$$

Where i stands for "initial", and refers to the particles on the left hand side of reaction 2.1, and f stands for "final" and refers to particles on the right hand side.

The reason why nuclear fission has been able to produce electric energy since the mid-20^{th} century is that it relies on reactions involving neutrons. In order for nuclei or nucleons to react via the strong force, it is necessary for them to reach distances from each other of the order of 1 fm (or 10^{-15} m). Having no electric charge neutrons can penetrate matter easily and can easily reach such distances from the target nuclei and this is probably the main factor that contributed to obtaining nuclear fission energy so much earlier than nuclear fusion energy, which has yet to be achieved. In the case of fusion, the two particles reacting are charged. The Coulomb potential between them is given by

$$V = k\frac{Z_1 Z_2}{r} \tag{2.3}$$

where Z_1 and Z_2 are the charges of the two particles, r is the distance between them, and k is a constant, depending only on the chosen system of units, equal to $8.99 * 10^9$ N $\mathrm{m}^2/\mathrm{C}^2$ in SI units. This electromagnetic interaction between the two reacting particles effectively leads to what is referred to as Coulomb barrier: a charged nucleus travelling towards another charged nucleus encounters a potential that rises as the distance between the two nuclei decreases, followed by a very deep potential well, caused by the strong nuclear force. While quantum tunneling allows for the fusion reactions to happen at kinetic energies that can be orders of magnitude smaller than the value provided by equation 2.3, it is still necessary for the relative velocity between the two nuclei to be very high. For the case of a reaction between deuterium (D) and tritium (T), the reaction has the highest probability to happen at energies of 64 keV. The reaction between Deuterium and Tritium is shown in equation 2.4

$$\mathrm{D} + \mathrm{T} \longrightarrow {}^{4}_{2}\mathrm{He} + \mathrm{n} + 17.6\,\mathrm{MeV} \tag{2.4}$$

In addition, in order for the reactions to take place efficiently and be used to produce energy it is in general necessary for all particles to have similar energies. For the case of DT, if we assume the fuel can be described by a Maxwell-Boltzmann distribution, the temperatures for such a distribution must be of the order of 10^6 K in order for the probability of the reaction to not be negligible. At these temperatures, matter is in the plasma state; in this state, a sufficient number of atoms is ionized, leading to behaviors that are wildly different from that of gases. The the main difficulty for nuclear fusion, is the necessity to contain plasmas at extreme temperatures.

There are two main approaches that have been developed in order to confine matter under such extreme condition, namely magnetic and inertial confinement. In magnetic confinement, the plasma is magnetically confined through the use of powerful magnets. In this approach, the goal is to reach a steady state, meaning that the plasma reaches an equilibrium configuration where it is continuously fusing and producing energy. The world's biggest machine of this type, by the name of ITER, is currently being constructed in southern france and is the fruit of the collaboration between many countries. The second approach does not aim to produce steady state conditions. In this approach, suggested first in 1972[29], small amounts of matter are compressed to high densities for the time interval in which inertia keeps the fuel burning together. This can be done by imploding spherical shells through the use of high-power radiation, delivered by an external driver, such as a laser or heavy ion beams. This scheme takes the name of inertial confinement fusion (ICF), and is the context for the current thesis work.

2.3 Inertial Confinement Fusion

In this chapter the fundamentals of ICFl be introduced and contextualized. The direct- and indirect- drive approaches are explained, and the two laser facilities performing ICF research in the USA are introduced, namely the National Ignition Facility and the Omega laser. Some of the advantages of the two approaches are introduced together with possible ways to increase the performance of the two facilities.

A typical target for ICF is shown in figure 2.2(a). It is composed of a shell of cryogenic deuterium and tritium (DT) ice, containing DT gas and surrounded by a thin layer of material, which is referred to as the ablator. In ICF a target is illuminated with a driver, such as lasers or beams of heavy ions[32], in order to quickly ablate the outside layer of material, thus imploding the DT shell via rocket effect. This causes strong shocks in the target, leading to an implosion which strongly compresses it and heats its center. If the target is compressed sufficiently at the moment of peak compression (stagnation), nuclear reactions begin in its center, creating the so called "hot-spot". The current goal of ICF is to achieve ignition: this refers to reaching a condition where nuclear fusion reactions are self sustained. In this condition, the alpha particles produced by fusion reactions in the hot-spot heat the remaining "cold" fuel causing an outward propagating fusion

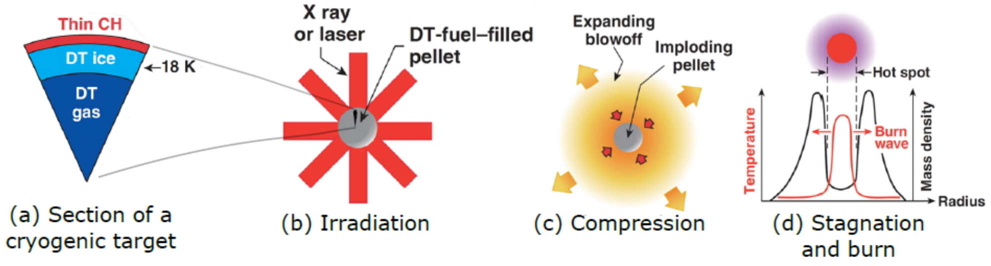

Figure 2.2: Illustrations of the main phases in an ICF implosion. The cryogenic DT target is compressed to high densities via the use of X-rays or lasers. This compression heats the target, specifically the core, to very high density, initiating fusion reactions. The goal is to compress the target to sufficiently high densities and temperatures to initiate a burn wave of fusion reactions, burning through the cryogenic shell. This illustration is taken from ref. [7].

burn wave. The long-term goal, necessary for producing electric energy, is to be able to obtain more energy than is put into the system. Early predictions for the laser energy necessary for achieving these goals were too optimistic, mostly because they underestimated the importance of hydrodynamic and laser-plasma instabilities (LPIs) occurring during the implosion.

Within the field of ICF there are two main possible approaches, which are known as direct and indirect drive. Both require high-power and high-energy lasers, but in the two approaches, the energy is transferred to the targets in different ways. As the name suggests, in direct drive implosions the laser illuminates the target directly, whereas in the indirect approach the laser is used to illuminate the walls of a high-Z cylinder containing the target, which takes the name of hohlraum. This causes the walls to emit black body radiation x-rays, and this x-ray "bath" drives the implosion. This appoach allows to obtain more uniform illumination of the target, reducing short-scale nonuniformities, but at the cost of coupling less energy to the imploding target.

There are a limited number of facilities in the world conducting ICF experiments; the main facilities pursuing this type of research in the U.S.A. are the Laboratory for Laser Energetics (LLE) and the National Ignition Facility (NIF). The Omega Laser Facility at the LLE houses the 60-beam OMEGA laser system. OMEGA is set up for direct-drive ICF experiments, with its 60 beams oriented in an icosahedral soccer ball pattern of hexagons and pentagons to minimize drive asymmetries. The OMEGA laser delivers

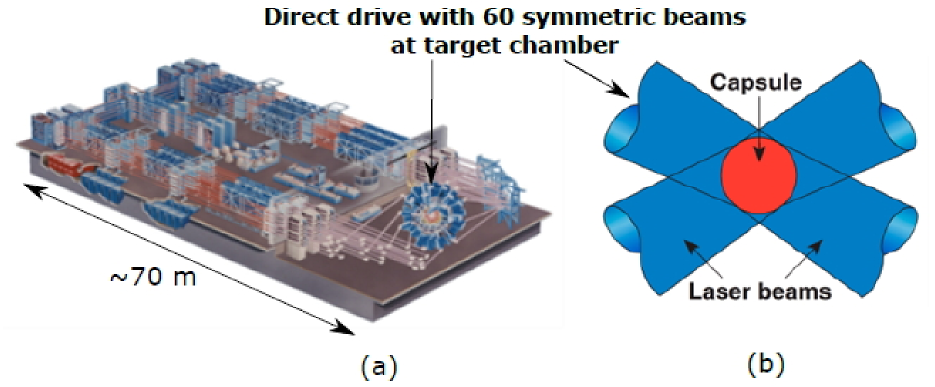

Figure 2.3: Illustration of the Omega laser bay and target chamber (a) and a schematic illustration of the concept of direct drive ICF (b). This illustration is taken from ref. [7].

up to 500 J per beam at a wavelength of 351 nm, in a variety of pulse shapes with a 4 ns maximum duration and a total peak power of 30 TW. With the capability of producing up to 30 kJ of laser energy on target Omega is the second most energetic direct drive laser facility in the world[38] and one of the most efficient, capable of performing several shots in a single day, The OMEGA laser and target bays are shown in figure 2.3. Some of the direct drive experiments performed in 2017 and early 2018 at the OMEGA laser facility are the best performing ones obtained on this facility by many metrics. In this thesis it will be shown that they are expected to produce over 250 kJ of fusion energy when scaled to NIF energies of 1.9 MJ. NIF is currently limited to perfroming polar direct drive experiments, which are believed to perform worse than spherically-symmetric direct drive. In polar direct drive experiments, the laser beams are reconfigured in order to mitigate the fact that NIF currently does not possess any laser beams on the equator; when it was built, NIF was set up in the polar drive configuration, suitable for indirect drive implosions, as shown in fig. 2.5 (c). OMEGA experiments on the other hand routinely use symmetric illumination, albeit with a smaller laser energy than NIF. In this thesis it will be shown that it's possible to obtain estimates for the performance of Omega implosions on NIF using a limited number or reasonable assumptions, and the technique for achieving this goal is described. Briefly, this process consists on a reconstruction of the implosion core and a subsequent upscaling to NIF energies and coditions

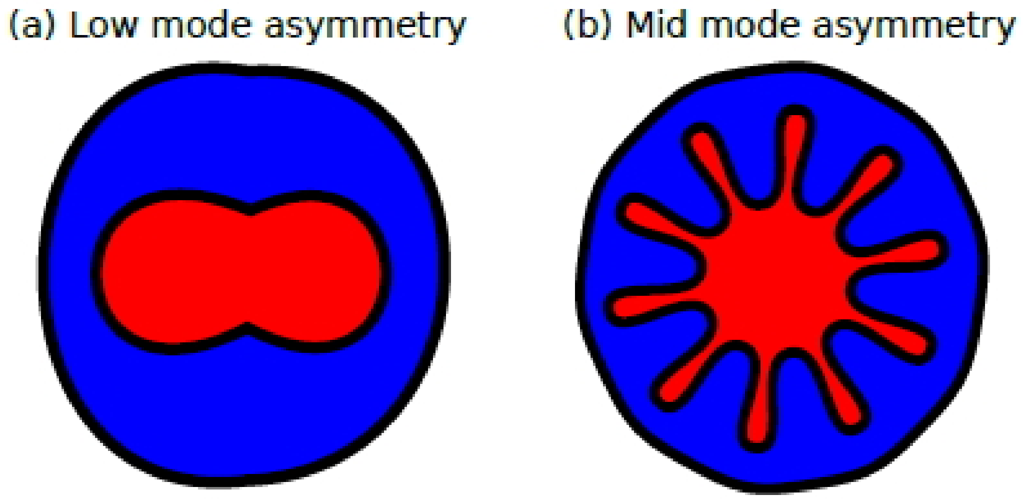

Figure 2.4: Depiction of the concepts of low (a) and mid-mode (b) asymmetries. While it is believed that the main asymmetries on indirect-drive NIF are of the former type, a direct drive configuration would cause a combination of both. This illustration is taken from ref. [7].

using the principle of hydrodynamic equivalency[28]. It is this technique that, applied to the forementioned shots performed on Omega, allows to obtain estimates of 250 kJ at NIF energies of 1.9 MJ.

In order to further improve the implosion performance on OMEGA, it is essential to analyze the experimental results for systematic trends in the experimental observables. This can be done only with carefully designed and controlled experiments with systematic changes of the target and/or laser parameters. Most likely degradation mechanisms for direct drive include mid mode asymmetries (see fig. 2.4), introduced by the beam port geometry of OMEGA and enhanced by LPI-induced cross beam energy transfer[16]. Low-mode asymmetries can be introduced by multiple mechanisms including the stalk holding the target in the target chamber, target offset and differences in laser beam power balance. Hot electron preheat is also a possible candidate for degradation in the implosion convergence. Recognizing and correcting the primary degradation mechanism would determine the path for direct drive towards demonstrating on OMEGA implosion performances that would hydro-equivalently scale to ignition at NIF energies.

The National Ignition Facility: The National Ignition Facility (NIF) laser

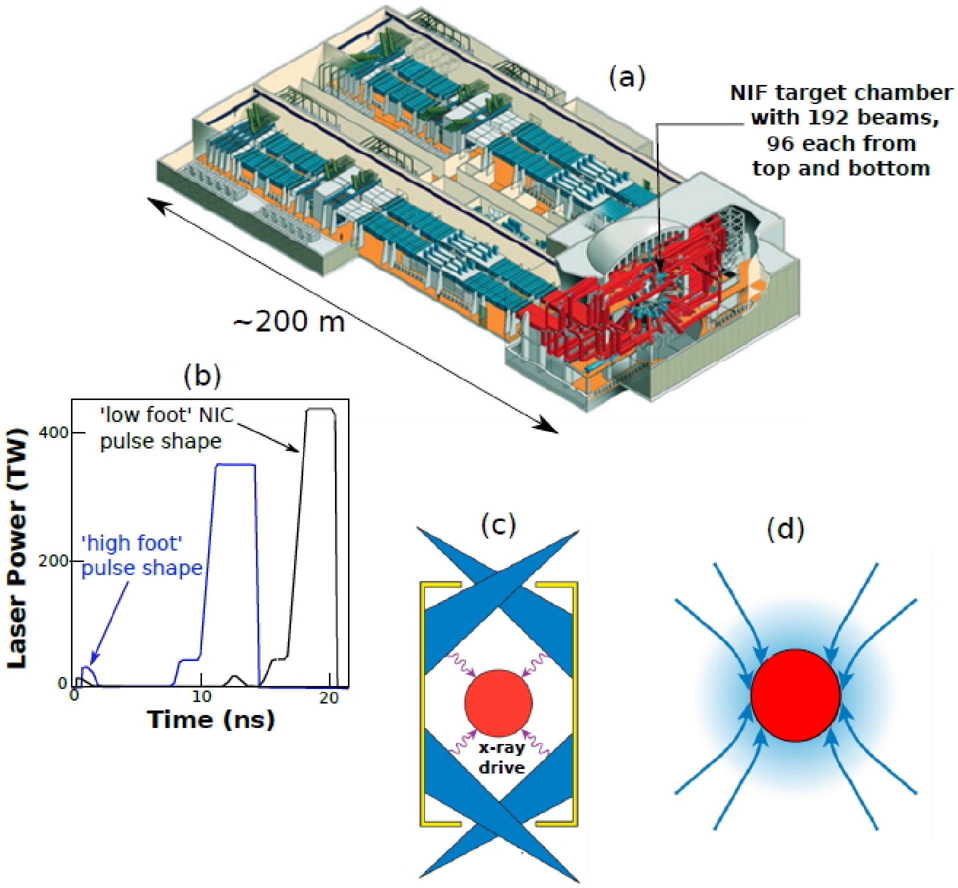
(a)
NIF target chamber with 192 beams, 96 each from top and bottom
~200 m
(b)
'low foot' NIC pulse shape
'high foot' pulse shape
Laser Power (TW)
400
200
0
0
10
20
Time (ns)
(c)
x-ray drive
(d)

Figure 2.5: This illustration is taken from ref. [7].

system, is shown in figure 2.5, located at the Lawrence Livermore National Laboratory (LLNL) is the largest laser facility in the world, and the most energetic ICF device built to date. NIF consists of 192 beams, divided into 48 quads of 4 beams each, delivering up to 2 MJ at a peak power of 500 TW. Typical laser pulses range from 1.4-to-20 ns in duration. Configured for indirect-drive ICF experiments, the beams are arranged into 4 rings at 23°, 30°, 45°, and 50° relative to the hohlraum axis. The laser power and wavelength can be adjusted from one ring to the next in an attempt to reduce the radiation flux asymmetry inside the hohlraum. Beam pointing can be adjusted slightly to allow for different experimental con

gurations, including the polar direct drive (PDD) configuration. In polar drive, the NIF beams are re-pointed to optimize the illumination uniformity for direct irradiation of an ICF capsule. Typical indirect-drive ICF experiments on NIF use Au or depleted uranium hohlraums of 10 mm length and 5.75 mm diameter, with a laser entrance hole at each end. Ignition-relevant capsules are spherical shells approximately 2.1 mm in diameter, consisting of a CH ablator surroundind a DT ice layer and filled with DT gas. The indirect drive experiments conducted in 2014 - 2017, at the LLNL, reached the highest level of alpha heating ever achieved on any facility based ICF experiments[19,15]. Self-heating by deposition of alpha particle energy is a key step on the path to ignition. Alpha particles are a product of DT fusion reactions and carry 3.5 MeV, out of the 17.6 MeV energy produced per fusion reaction, in the form of kinetic energy. In these experiments the alpha particles deposited their energy within the hot spot, thereby doubling the fusion yield. It was estimated that the fusion yield produced exceeded the yield produced from the work done by the compression of the fuel alone. The success of the "high foot"[20](HF) experiments spurred from modifications of laser pulse shape, shown in fig. 2.5(b). The initial picket of the laser pulse was approximately doubled in power as compared to the low foot drive performed earlier during the National Ignition Campaign (NIC). This resulted in a reduction of hydrodynamic instabilities caused by the higher shell entropy at the price of a reduced fuel convergence. The series of HF implosions achieved the highest fusion-energy yield, 26 kJ in 2014 and 50 kJ in 2017. The major challenge for indirect drive is to provide a uniform x-ray intensity on the capsule surface. The hohlraum introduces low mode asymmetries to the implosion, illustrated in fig. 2.4(a). Improving the core asymmetries arising from a nonuniform x-ray illumination, along with reducing the degradation caused by engineering features, such as the "tent" which holds the target in the hohlraum,are required for improving the implosion performance.

2.4 Basic Concepts in ICF Theory

In the current chapter, a more detailed introduction than the one given in the previous section is provided. In particular, several technical concepts are introduced. After briefly introducing the equations determining the evolution of an ICF implosion are introduced, important concepts connected to the laser pulse and to the entropy of the shell are introcuded and contextualized. Some formulae to estimate important parameters for a given ICF implosion are illustrated. This section is only meant to provide the reader with an overview of ICF on more quantitative terms than the previous section, but it is not expected to be a complete description of all ICF topics, which can be found for instance in the book by Atzeni[1].

The fuel for ICF consists in a mixture of deuterium and tritium, which can react according to reaction 2.4. It can be shown using the conservation of energy and of momentum that the energy in the products is distributed as follows: 14.1 MeV is the kinetic energy of the neutron, while 3.5 MeV is the kinetic energy of the alpha particle. The neutron has no charge and has very small cross sections for reacting with the nuclei present in the plasma and therefore will not deposit its energy within the plasma. The alpha particle, on the other hand, is charged and transfers its energy to the electrons in the plasma, which in turn transfer their energy to the ion populations, thus contributing to keeping the plasma at fusion temperatures.

The ignition condition is defined as the condition under which the plasma is self sustaining, i.e. can maintain itself at high temperatures. This condition is defined by the requirement

$$P\tau > 10\text{atm s or } 10 \text{ Gbar ns}, \tag{2.5}$$

where P is the pressure of the plasma (in atmospheres) and τ is the confinement time. This can lead to very different approaches: magnetic confinement aims at reaching the ignition condition with plasmas of pressures of the order of ~ 1 atmospheres and a time of the order of 1 second, while in inertial confinement the pressure is of the order of several Gbar, with times of the order of the nanosecond. Both approaches reach similar temperatures of $\sim 10^8$ K. In ICF, these conditions can be reached through the use of laser-driven spherical implosions of a thin shell of solid DT, filled with DT gas. Targets have radii of the order of 1 mm, and consist in an outside layer, the ablator, covering the layer of DT ice, which in turn contains the DT gas. The ablator usually is made of CH (i.e. plastic) or Berillium.

In order to model an ICF implosion, it is necessary to have a model for the DT plasma. For the purposes of this introduction, the model is based on the conservation equations of gas-dynamics, in one dimension, coupled with the idel gas equation of state. These are:

$$\begin{aligned} \partial_t\rho + \partial_x(\rho v) &= 0, \\ \partial_t(\rho v) + \partial_x(p + \rho v^2) &= \text{body forces (e.g: } \rho\vec{g}), \\ \partial_t\varepsilon + \partial_x[v(\varepsilon + p) - k\partial_x T] &= \text{sources + sinks}, \\ p = (n_e T_e + n_i T_i) = 2nT &= (\frac{2}{m_i})\rho_i T, \end{aligned} \tag{2.6}$$

where in the last equation it was assumed that $T_e = T_i = T$ and $n_e = n_i = n$ (for DT plasmas, with Z = 1), where T and n are the temperature and particle density respectively. ρ is the mass density ($\rho = n_i m_i$), p is the total pressure, ε is the total energy per unit volume, equal to $\varepsilon = 3/2p+\rho\frac{v^2}{2}$ for the case of an ideal gas, and lastly k is the plasma thermal conductivity, which is approximated as $k \approx k_0 T^{5/2}$.[35] In addition to these equations, it is necessary to model the laser-plasma interaction. The laser light cannot propagate past the critical density: this is because at the critical density the laser frequency is the same as the electron plasma frequency ($\omega_L^2 = \omega_{pe}^2$, where $\omega_L = \frac{2\pi c}{\lambda_L}$ is the laser frequency and $\omega_{pe} = \sqrt{\frac{4\pi n_e e^2}{m_e}}$ is the electron plasma frequency) and this causes a resonant absorption of the laser energy; for distances further than r_{cr} the amplitude of the laser is exponentially decaying. A simple relation to determine the critical electron density is:

$$n_e^{cr} = \frac{1.1 * 10^{21}}{\lambda_L(\mu m)^2} cm^{-3}. \tag{2.7}$$

The laser deposits its energy near the critical surface, at $x = x_c$; for distances between x_c and the ablation front, heat flows by conduction, and for this reason this region is called the conduction zone. The ablation front moves inwards at a velocity of v_a = ablation velocity.

An important topic to be addressed is the concept of entropy. It plays a key role in ICF implosions, most importantly because matter is compressed to extreme densities and high entropy targets require more energy to be compressed than low entropy ones. This will be shown with the simple reasoning in equation 2.10. The entropy is defined as

$$S = c_v \ln[\frac{p}{\rho^{5/3}} const] = c_v \ln[\alpha], \alpha = const\frac{p}{\rho^{5/3}}. \tag{2.8}$$

α is defined as the "adiabat". The entropy and the adiabat change because of dissipation, heat sources or sinks. In an ideal gas (which has no dissipation) and without sources and sinks S and α are constants of motion of each fluid element, i.e.:

$$\frac{DS}{Dt} = 0 \Rightarrow S, \alpha = const \Rightarrow p \sim \alpha \rho^{5/3}. \tag{2.9}$$

A low adiabat gas is easier to compress:

$$W_{12} = -\int_{\rho_1}^{\rho_2} pdV \sim -\int_{\rho_1}^{\rho_2} \alpha \rho^{5/3} d\frac{M}{\rho} \sim \alpha M(\rho_2^{2/3} - \rho_1^{2/3}). \tag{2.10}$$

In HEDP the constant for the definition of the adiabat comes from the normalization of the pressure to the Fermi pressure, leading to, for the case of DT,

$$\alpha_{DT} \equiv \frac{p(Mb)}{2.2\rho(g/cm^3)^{5/3}}. \tag{2.11}$$

In ICF the implosion is very rapid and generally launches multiple shock waves in the target, and these can cause significant changes in the value of the adiabat. The shound speed in a gas or plasma is $\sim \sqrt{p/\rho} \sim \sqrt{\alpha\rho^{2/3}} \sim \sqrt{\alpha}\rho^{1/3}$. Therefore if the gas or plasma is quickly compressed, the waves launched in it overlap due to the increasing sound speed with density; this overlap causes a steepening and eventually a discontinuity in the hydrodynamic properties. This is a shock. The flow of mass, momentum, and energy is conserved across the shock front, leading to the Rankine-Hugoniot conditions:

$$\begin{aligned} \rho_1 u_1 &= \rho_2 u_2, \\ p_1 + \rho_1 u_1^2 &= p_2 + \rho_2 u_2^2, \\ u_1(\varepsilon_1 + p_1) &= u_2(\varepsilon_2 + p_2), \end{aligned} \tag{2.12}$$

where ρ_i, p_i u_i are the densities, pressures, and velocities of the fluids on the two sides (denoted as 1 and 2) of the shock (as in figure 2.6). ε for an ideal gas, as previously mentioned, is equal to $\varepsilon = 3/2p + \rho\frac{v^2}{2}$. In the case of a strong shock, for which $p_2 >> p_1$, the equations simplify. The simplified system of equations provides simple relations for the velocity of the shock (equal and opposite to u_1, the velocity u_2, and the ratio of $\frac{\rho_2}{\rho_1}$. This last expression in particular is surprisingly simple:

$$\frac{\rho_2}{\rho_1} \approx 4. \tag{2.13}$$

Calculating the ratio between the adiabat in the two regions in this case, obtained simply by using the definition of adiabat and the result of equation

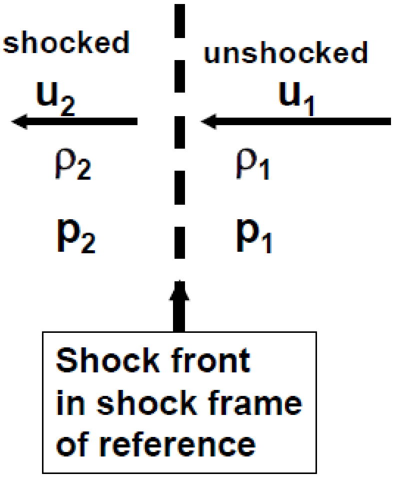

Figure 2.6: Schematic representation of the properties of a fluid on the two side of a shock front.

2.13, the following result can be obtained:

$$\frac{\alpha_1}{\alpha_2} = \frac{1}{4^{5/3}} \frac{p_2}{p_1} >> 1. \tag{2.14}$$

This last result provides an important conclusion: the adiabat increases significantly through a shock. Therefore equation 2.11 can be simplified, by substituting to ρ_2 the value of $4\rho_1$. The result in equation 2.14 can be used to reach some simple conclusions regarding the laser pulse shape, illustrated in figure 2.7, which also shows the main characteristics and nomenclature for a standard laser pulse. In order to accelerate to high velocities without significantly increasing the adiabat, it is necessary, after the first shock, to slowly increase the intensity, in order to prevend further shocks from developing and further increasing the adiabat. In addition some general conditions hold for an optimal laser pulse; it is found that starting this increase at half of the shot breakout time t_{sb}, defined as time required for the shock to reach the rear target surface, and ending it at t_{sb} prevents rarefaction wave to propagate back from the rear target surface and consequently decompressing the target. Most of the laser energy that is absorbed by the plasma is transferred into kinetic and thermal energy of the expaning, blow-off plasma, rather than into kinetic energy of the imploding shell. A model that can be used to describe

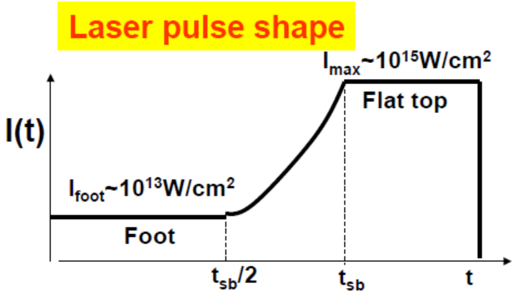

Figure 2.7: Schematic representation of laser pulse for an ICF implosion. t_{sb} stands for shock breakout time, and refers to the time required for the shock to reach the rear target surface. The laser pulse shown here is a typical configuration, consisting of a low intensity "foot", followed by a smooth increase to the full laser intensity, which is then maintained in order to further increase the convergence of the target, defined as the ratio of the initial shell radius and the size of the hotspot, leading to a "flat top". The intensities shown are typical intensities for ICF laser pulses.

the absorption of the laser energy is the rocket model:

$$\begin{aligned} M\frac{du}{dt} &= -4\pi R^2 P_a, \\ \frac{dM}{dt} &= -4\pi R^2 \dot{m}_a, \\ P_a &= \dot{m}_a u_{exhaust}, \end{aligned} \tag{2.15}$$

In this model, the first equation is the Neuton law written for the shell, the second represents the shell mass decrease due to ablation, and the third equals the ablation pressure to the ablation rate times the exhaust velocity. This model can be useful to estimate the value of the hydro-efficiency, defined as $\eta_h = \frac{E^{shell}_{kinetic}}{E_{exhaust}}$. It is found that the efficiency is maximum for $M_{final} \sim 0.2 M_{initial}$. For direct drive ICF $\eta_h \sim 8-10\%$.

These are some of the many concepts that are necessary to fully describe and analyze an ICF implosion. Many aspects of physics have to be modeled in order to obtain predictions for actual ICF implosions. These go from laser-matter interaction, to hydrodynamics, to high energy density physics (HEDP, the branch of physics studying matter under extreme conditions) and more. For these reasons ICF implosions are constantly used to obtain a better understanding all of the physics involved, and are an invaluable research tool for all these areas of physics and engineering.

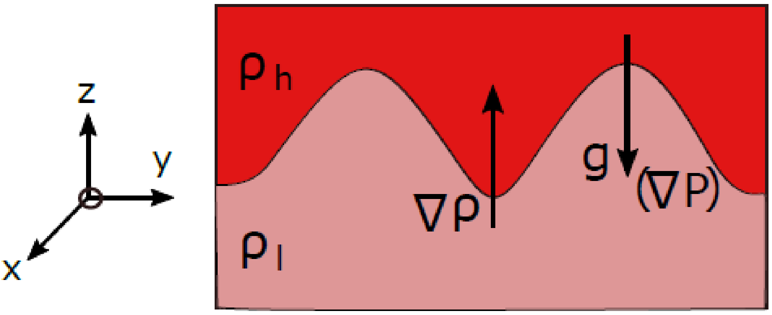

Figure 2.8: Schematic view of a RT unstable system, i.e. a system for which $\nabla\rho\cdot\nabla P < 0$. The pedices "h" and "l" refer to "heavy" and "light" densities. The equilibrium pressure is given by $P_0(z) = Const. - \rho_0 g z$, with $\rho_0 = \rho_h$ for $z > 0$ and $\rho_0 = \rho_l$ for $z < 0$, and must be continuous at the interface. The image is adapted from ref. [7]

2.5 Implosion and Instabilities

There are two phases during an ICF implosion in which Rayleigh-Taylor instabilities (RTI) play a role: these are the acceleration and the deceleration phase. In the former case, it is the outer surface of the shell that is subject to RTI, while in the latter it's the inner,i.e.the hot-spot and shell interface surface that is unstable. For the latter case, this effect leads to asymmetries in the hot-spot compression and degrades the implosion performance. In this chapter a brief description of the RTI phenomenon is provided, as it plays a key role in the numerical study performed in chapter 3.

Hydrodynamic systems are unstable to the RTI if they experience opposite density gradient and acceleration at an interface. The general condition for the instability is given by $\nabla\rho \cdot \nabla P < 0$. A simple example of such a situation is shown in figure 2.8. Stated simply, if a lighter fluid is accelerated towards a denser fluid: as previously mentioned this happens in two parts of an ICF implosion; in the acceleration phase, the light fluid is the coronal plasma accelerated towards the shell (i.e. it "pushes" the shell), and the same happens during the deceleration phase, but in this case the light fluid is the hot-spot plasma. Such a situations represents unstable equilibria: perturbations of the interface grow exponentially with time in the linear regime. The perturbation amplitude $h(t) \sim h_0 e^{\gamma t}$, where γ is the linear growth rate of the RTI and h_0 is the initial amplitude of the perturbation. The classical growth rate is given by

$$\gamma_{RT} = \sqrt{Akg} \tag{2.16}$$

where $A = (\rho_h - \rho_l)/(\rho_h + \rho_l)$ is referred to as the Atwood number, g is the magnitude of the acceleration and $k = 2\pi/\lambda$ is the wave number of a pertubation with wavelength λ. This result can be obtained starting from:

$$\begin{aligned} \partial_t \rho + \nabla \cdot (\rho \vec{v}) &= 0 \\ \rho \partial_t \vec{v} + \rho \vec{v} \cdot \nabla \vec{v} &= -\nabla P + \rho \vec{g} \\ \nabla \cdot \vec{v} &= 0 \end{aligned} \tag{2.17}$$

namely the system of equations given by the conservation equations for mass, momentum, and the incompressibility condition. With this last equation it's possible to obtain a general formula for the growth rate, namely equation 2.16, but for more complex physical situations the full energy conservation equation is necessary. To obtain equations 2.17 a constant acceleration like the one present in figure 2.8 has been applied to the system. Using linear analysis, therefore assuming small perturbations around an equilibrium condition, all quantities can be written as $Q = Q_0 + Q_1$, where 0 stands for 0^{th} order (i.e. the equilibrium condition), 1 refers to 1^{st} order quantities, which we assume to be small. We consider the equilibrium with $\vec{v_0} = 0$. Additionally, in the simple case being studied, $\rho_0 = \rho_0(z)$, and takes on only two values, namely $\rho_0 = \rho_h$ for $z > 0$ and $\rho_0 = \rho_l$ for $z < 0$, and $\nabla P_0 = \rho_0 \vec{g}$. Substituting these considerations in the system of equations 2.17 the following system is obtained:

$$\begin{aligned} \partial_t \rho_1 + \vec{v_1} \cdot \nabla \rho &= 0 \\ \rho_0 \partial_t \vec{v_1} &= -\nabla P_1 + \rho_1 \vec{g} \\ \nabla \cdot \vec{v_1} &= 0 \end{aligned} \tag{2.18}$$

This problem can be formulated as a normal mode problem; the first step is the separation of variables, namely $Q_1 = \hat{Q}_1(z) e^{i\vec{k}\cdot\vec{x}+\gamma t}$. This can be then simplified by taking $\vec{k} = k_x = k > 0$ and $k_y = 0$. With these assumptions equations 2.19, denoting $D_z = \mathrm{d}/\mathrm{d}z$, reduce to the a set of four equations:

$$\begin{aligned} \gamma \hat{\rho}_1 + \hat{v_1}_z D_z \rho_0 &= 0 \\ \gamma \hat{\rho}_0 \hat{v_1}_x &= -ik\hat{P}_1 \\ \gamma \hat{\rho}_0 \hat{v_1}_z &= -D_z \hat{P}_1 - \hat{\rho}_1 g \\ ik\hat{v_1}_x + D_z \hat{v_1}_z &= 0 \end{aligned} \tag{2.19}$$

These can be combined to obtain an equation for $\hat{v_{1z}}$, leading to

$$k^2\rho_0\hat{v_{1z}} = D_z(\rho_0 D_z\hat{v_{1z}}) + \frac{k^2}{\gamma^2}g\hat{v_{1z}}D_z\rho 0 \tag{2.20}$$

which can also be written as

$$[D_z^2 - k^2 + \frac{D\rho_0}{\rho_0}(\frac{gk^2}{\gamma^2}) + D_z]\hat{v_{1z}} = 0. \tag{2.21}$$

For $z \lesseqgtr 0$ $D_z\rho_0 = 0$, as a consequence of the fact that the density is assumed constant for $z \lesseqgtr 0$, reducing equation 2.21 to:

$$[D_z^2 - k^2]\hat{v_{1z}} = 0 \tag{2.22}$$

to be evaluated in the two regions $z \lesseqgtr 0$. The solution to these two equations can be written compactly as

$$\hat{v_{1z}} = \begin{cases} Ce^{-kz} & \text{for} z \geqslant 0 \\ Ce^{kz} & \text{for} z \leqslant 0 \end{cases} \tag{2.23}$$

and must be continuous at the boundary. γ can now be found by evaluating the jump condition across the interface; this is done by integrating equation 2.20 in the infinitesimal interval $-\varepsilon \leqslant z \leqslant \varepsilon$, leading to

$$\int_{-\varepsilon}^{\varepsilon} k^2\rho_0\hat{v_{1z}}dz = \int_{-\varepsilon}^{\varepsilon} \mathrm{d}/\mathrm{d}z(\rho_0\mathrm{d}/\mathrm{d}z\hat{v_{1z}})dz + \int_{-\varepsilon}^{\varepsilon} \frac{k^2}{\gamma^2}g\hat{v_{1z}}\mathrm{d}/\mathrm{d}z\rho_0, \tag{2.24}$$

where D_z is expressed as $\mathrm{d}/\mathrm{d}z$ for clarity, which in turn leads to

$$k^2C(\rho_h + \rho_l)\varepsilon = -(\rho_h + \rho_l)kC + \frac{k^2}{\gamma^2}gC(\rho_h - \rho_l). \tag{2.25}$$

Making the substitution $A = (\rho_h - \rho_l)/(\rho_h + \rho_l)$, the expression in equation 2.16 is obtained. It should be pointed out that A is positive, and therefore γ is real. If the position of the regions with densities ρ_h and ρ_r in figure 2.8 were inverted, an imaginary γ would be obtained; therefore the behavior would be oscillatory, but stable.

This has been a simple derivation relying on a discontinuous density.

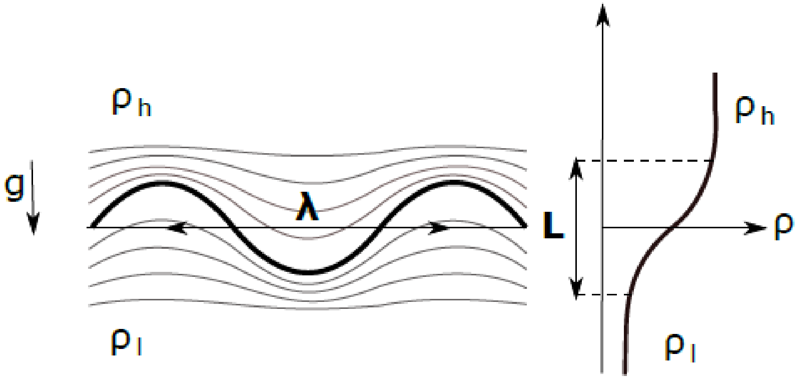

Figure 2.9: Perturbed interface between a heavy fluid with density ρ_h supported by a lighter fluid with density ρ_l(left). The perturbation has a wavelength = λ. On the right the profile of the density as a function of z is plotted, showing a characteristic scale length of L. The image is adapted from ref. [7]

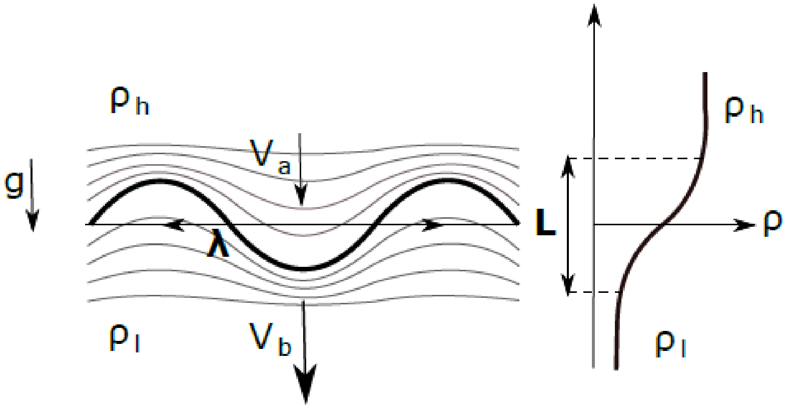

Figure 2.10: Perturbed interface between a heavy fluid with density ρ_h supported by a lighter fluid with density ρ_l(left). The perturbation has a wavelength = λ; mass ablation causes the diffused density profile on the right, showing a characteristic scale length of L. Transitioning to the reference frame of the interface, the heavy fluid moves towards it with the ablation velocity v_a, crosses the interface, and blows off into the low density region with a higher velocity (v_b, blow-off velocity). The image is adapted from ref. [7]

The effect of a smoother density profile, such as the one in figure 2.9, or of a moving interface, such as the one in figure 2.10 lead to changes in γ; It is found[36,37] that:

$$\gamma \approx \alpha\sqrt{\frac{kg}{1+kL}} - \beta v_a, \tag{2.26}$$

where $\alpha \simeq 0.9-1$, $\beta \simeq 3-4$, v_a is the ablation velocity, and L is a characteristic scale length corresponding to the continuous density transition region. It is evident that increasing L and v_a the growth rate is reduced, and can even become negative, leading to stable perturbations.

During the deceleration-phase of ICF implosions the heat- and radiation-flux coming from the hotspot causes mass ablation at the interface. Transitioning to the reference frame of the ablation front (i.e., the interface) the heavy fluid moves towards it with the ablation velocity, crosses the interface, and is blown off into the low density hot-spot with a blow-off velocity that is higher than the ablation velocity. Ablation at the hot-spot shell interface has a very similar mitigating effect on the deceleration phase RTI as in the equation 2.26. The RTI during the deceleration phase (dp) and the ablative stabilization has been studied theoretically by Lobatchev and Betti[26], Shvartz et al.[24], and many others.

Chapter 3

Trends in Experiments and Recontruction of the Implosion Core

3.1 Introduction

This chapter shows the method involved and the results from the reconstruction of the experimental observables for the high adiabat (i.e. low converging) cryogenic implosions on OMEGA. This is essential for the extrapolation of the implosion core to NIF scale and estimation of the performance of direct drive implosions at NIF energies.

The laser drive was simulated using the 1-D hydrodynamic code LILAC [14]. It was observed that the results from the hydrodynamic simulations need to be degraded significantly in order to match the experimental observables. The difference between the 1-D simulation results and the experiments are compensated through a heuristic degradation in the laser pulse shape in the LILAC simulation results, and a 2-D distortion of the implosion core caused by the Rayleigh-Taylor instability growth. The former is discussed in section 3.2 where the experimental results are shown and are compared with the 1-D LILAC calculations. The latter is discussed in section 3.4 where the 1-D results are further degraded in 2-D.

The 1-D code LILAC includes models for laser absorption which drives the capsule,diffusion model for thermal conduction,[18] multi group diffusion model for radiation transport,and equation of state models for the plasma at

Table 3.1: This table shows the experimental results (exp.), compared with the results from the original 1-D simulation (LILAC) and the best reconstruction found for the two shots analyzed (comp.), 87266 and 88314. Part I

Shot Number	**Ion Temperature** [keV]	**Hotspot Radius** [μm]	**Areal Density**[mg/cm^2]	
87266, Exp.	4.51 ± 0.32	33.1 ± 0.7	97 ± 9	100 ± 14
87266, LILAC	5.71	27.2	136	
87266, Comp.	4.04	31.1	105	101
88314, Exp.	4.32 ± 0.30	31.4	115 ± 10	138 ± 19
88314, LILAC	5.79	24.0	183	
88314, Comp.	4.52	25.3	137	133

Table 3.2: This table shows the experimental results (exp.), compared with the results from the original 1-D simulation (LILAC) and the best reconstruction found for the two shots analyzed (comp.), 87266 and 88314. The two value for the areal density correspond, in order, to MRS and ntof measurements. Part II

Shot Number	**Yield** [10^{14}]	**Pressure** [Gbar]	**Burn Width** [ps]	**Bang Time** [ns]
87266, Exp.	1.34 ± 0.1	35.5	81 ± 8	2.193 ± 0.05
87266, LILAC	5.53	95.0	57	2.097
87266, Comp.	1.34	42.2	87	2.151
88314, Exp.	1.28 ± 0.06	40.2	78 ± 8	2.155 ± 0.05
88314, LILAC	7.81	139.5	53	2.170
88314, Comp.	1.31	56.9	70	2.185

extreme conditions.The LILAC simulations used in this thesis are described in section 3.3. The explanation for the significant differences between the experiment and the data from the 1-D simulations is provided, which suggest that there might be a deficiency in the laser coupling model in LILAC. In other words the interaction between the laser and the target is not modeled accurately. However, the differences may also arise from inaccuracy in the other models used in LILAC. For the purposes of this thesis, a simple ad-hoc mechanism is explored in order to provide a degraded simulation which is comparable to the experiments, the degradation involved relies on modifications of the laser pulse shape. This couples less energy to the target and it is shown that this can produce a reasonable agreement with experimental results.

In section 3.4, the 1-D degraded simulations are further degraded in 2-D via the use of specific perturbation modes, using the radiation hydrodynamics code DEC2D. The main characteristics of this code are illustrated in this section. Subsequently, the trends in implosion observables arising from the perturbations of different wavelength are analyzed in order to reproduce the experimental results, i.e. reconstruct the implosion core in simulations.

Lastly, in section 3.5, a comparison between the experiment and the reconstructed simulations is provided; the small differences between the experimental results and the degraded simulations are discussed with appropriate justification.

3.2 Experimental results for 87266 and 88314

Of all the cryogenic shots performed on Omega, this thesis focuses on shot 87266 and 88314. These were chosen because they are currently two of the performing shots performed on Omega, as a part of an optimization campaign with the goal of optimizing pulse shape and target dimensions to get the highest possible values for implosion performance metric and yield. 87266 is the best shot in terms of absolute neutron yield, while 88314 is the shot with the highest areal density among the shots with highest yield.

Tables 3.3 and 3.4 show the main experimental observables and their counterparts from the corresponding 1-D simulations for shots 87266 and 88314. Ion temperature and areal density are neutron averaged quantities,

Table 3.3: Experimental results with the corresponding clean LILAC simulation, part I

Shot Number	**Ion Temperature** [keV]	**Hotspot Radius** [μm]	**Areal Density**[mg/cm^2]	
87266, Exp.	4.51 ± 0.32	33.1 ± 0.7	97 ± 9	100 ± 14
87266, LILAC	5.71	27.2	136	
88314, Exp.	4.32 ± 0.30	31.4	115 ± 10	138 ± 19
88314, LILAC	5.79	24.0	183	

Table 3.4: Experimental results with the corresponding clean LILAC simulation, part II

Shot Number	**Yield** [10^{14}]	**Pressure** [Gbar]	**Burn Width** [ps]	**Bang Time** [ns]
87266, Exp.	1.34 ± 0.1	35.5	81 ± 8	2.193 ± 0.05
87266, LILAC	5.53	95.0	57	2.097
88314, Exp.	1.28 ± 0.06	40.2	78 ± 8	2.155 ± 0.05
88314, LILAC	7.81	139.5	53	2.170

and are calculated in the following way

$$Q_{navg} = \frac{\int dt \int dV n_D n_T \langle \sigma v \rangle Q}{\int dt \int dV n_D n_T \langle \sigma v \rangle}. \tag{3.1}$$

These can fairly easily be ontained in experiment, since they rely on neutron measurements. The hotspot radius is defined as the radius where the intensity of the X-rays due to bremsstrahlung drops below $1/e$ the maximum intensity at stagnation time, while the pressure is inferred from the other experimental observables[11]. The burn width and bang time are calculated from the gaussian fit of the experimental values of the neutron rate; the burn width corresponds to the FWHM of the gaussian, while the bang time is defined as the interval between when the laser first reaches 2% of the peak power and the time corresponding to the maximum in the gaussian. A comparison of experimental and 1-D simulation observables shows that yields, temperatures, pressures and areal densities are overestimated while radii and burn widths are underestimated. As far as the bang times are concerned, for 87266 the simulation predicts an earlier bang time with respect to experiment while for 88314 the predicted bang time is slightly late compared to experiment. It is important to notice that the bang times are affected by significant uncertainties. Most of these differences, except for differences in bang times for 88314, can be reduced via a 1-D degradation mechanism, as will be shown in section 3.3. The smaller remaining differences can be reduced by introducing 2-D perturbations at the start of the deceleration phase, as will be illustrated in

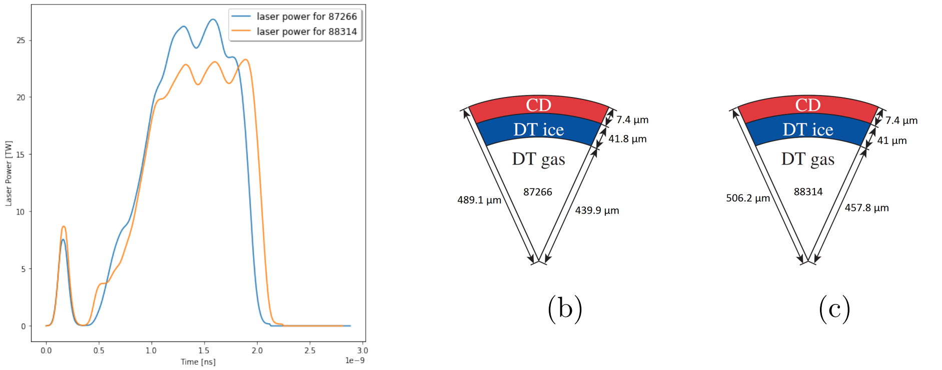

(b) (c)

(a)

Figure 3.1: Laser pulses and target dimensions for shots 87266 and 88314

section 3.4.

Figure 3.1 shows the laser pulses and target specifications for the two shots. From 3.1 (a) it can be seen that both pulses have a single picket and have similar shapes, but there are some noteworthy differences; the laser pulse used for 88314 is characterized by a slightly higher picket (8.7 TW compared to 7.5 TW for 87266), a longer pulse (2.2 ns compared to 2.1 ns), a more pronounced foot, a lower peak intensity (23.3 TW, compared to 26.8 TW) and, consequently, a lower average drive (21.9 TW compared to 25.1 TW). Although 88314 has a higher picket, the lower foot caused it to have an adiabat of only 3.7. This is lower than the value of 4.6, obtained in the 87266 implosion, and resulted in a higher convergence in the implosion, causing a smaller hotspot radius and higher areal density for 88314. These adiabat values are defined as the ratio of the hydrodynamic pressure (P) and the Fermi pressure of a degenerate electron gas (P_f), at the interface of the hot spot and shell at the time when the laser-driven shock reach this interface, i.e., $\alpha \equiv P/P_f$. While differences in the laser pulse are present, the laser energy for these shots was close: 28.022 kJ for 87266, 27.950 kJ for 88314. As evident from figures 3.1(b) and 3.1(c) the targets have the same composition and very similar dimensions. Both of these targets have a large outer diameter compared to the shots studied in ref. [7]. Altough the ice thickness is is slightly higher for 87266, its totall mass is lower than 88314 because of its smaller size. Other shots with similar target and laser configurations were performed, and several obtained yields of the same order of magnitude, but these were overall the best performing ones.

3.3 1-D Reconstruction of the Implosion Core

The 1-D code used for the purposes of this thesis work is LILAC. The main physics models used are the following:

- Laser deposition is modeled to account for the effect of cross-beam energy transfer (CBET)[21]. This effect is caused by beam overlap and is accounted for via a ray-tracing model; when using ray-tracing, the laser beams are decomposed into a finite number of rays and each of these is tracked in time. In the simplest case the rays deposit all of their energy once they reach the critical surface. LILAC accounts for CBET, making it possible for the rays to interact with each other[22]. The main effect of this is that less energy is coupled to the target.

- The equation of state used is derived from first principles (FPEOS for first principle equation of state);

- The hydrodynamic part of the code relies on a lagrangian finite difference scheme.

- Thermal conductivity relies on a nonlocal model, which provides more accurate results than thermal diffusion. In thermal diffusion $\vec{Q_l} = -k\nabla T$, therefore the heat flux only depends on the local temperature. In non local models, in general, $\vec{Q_{nl}} = \int_{-\infty}^{+\infty} W(r', r)\vec{Q_l}(r')dr'$, where $W(r', r)$ depends on the nonlocal model. Evidently this formulation is very general, and with the choice of $W(r', r) = \delta(r' - r)$ reduces to the local model.

- For the OMEGA scale implosions alpha particles don't deposit their energy in the target because of the relatively small yield of 10^{14} alpha particles and low areal densities.

In the precursor to the current thesis work, ref. [7],the 1-D degradations were dealt with by reducing the velocities to be imported in DEC2D from the LILAC profile by a factor slightly smaller than one, in order to cause a small shift in the simulated bang time. A similar approach was attempted for the purposes of this thesis for shot number 87266, but even with a factor much smaller than one, it was impossible to explain such a delayed experimental bang time. Therefore a different approach was developed to simulate a 1-D degraded implosion. Three different types of ad-hoc, 1-D degradation mechanisms were tested, all relying on variations to the original pulse shape in order to reduce the total laser energy. The modifications studied were the following:

1. reductions in the length of the laser pulse;
2. reductions in the maximum power of the laser;
3. a combination of the above

In order to do 1 the laser power is set to zero for all times after the moment when the laser energy reaches a given value; the variable in this case is the total laser energy, henceforth referred to as E_{cutoff}. For case 2, the variable was the maximum laser power, P_{cutoff}; this was imposed by "cutting" the part of the laser pulse above a given power, and resulted in laser pulses with a flat top. In the 3 case the variables were both E_{cutoff} and P_{cutoff}. Since most of the other observables can be heavily affected by different types of 2-D perturbation and therefore could be accounted for by using such a degradation, the most important observables to be matched with these 1-D degraded simulations were bang times and burn widths; therefore a systematic study of the simulations with these new profiles was conducted in order to try to match bang times and burn widths with their experimental counterparts, within a range of ±50 ps for the bang times, and of ±8 ps for the burn widths (these correspond to the error bars on the experimental measurement). The first two plots in figures 3.2 through 3.5 show the trends in the deltas between experimental and LILAC values for bang times and burn widths; figures 3.2 and 3.3 correspond to modifications of type 1 and 2, respectively, for 87266. Figures 3.4 and 3.5 correspond to modifications of type 1 and 2, respectively, for 88314. In all plots inf fig.s 3.2 through 3.5, the blue curve is obtained by linear interpolation between the values obtained from various LILAC simulations, with different values of E_{cutoff} and P_{cutoff}, while the two red bars correspond to the experimental values, plus or minus the error. For all (g) plots, there is no straightforward definition of the error, and therefore only a single red line is shown, corresponding to the inferred value of the pressure. Looking at the trends in all (a) and (b) plots, for both 87266 and 88314 it is evident that, for equal shifts in bang time, changes in the laser shape of type 1 have a stronger effect on the burn width with respect to changes of type 2. For instance, for 87266, a perturbation of type 1 that gives a shift in bang time of about 40 ps also gives an increase in burn width of 45 ps, whereas

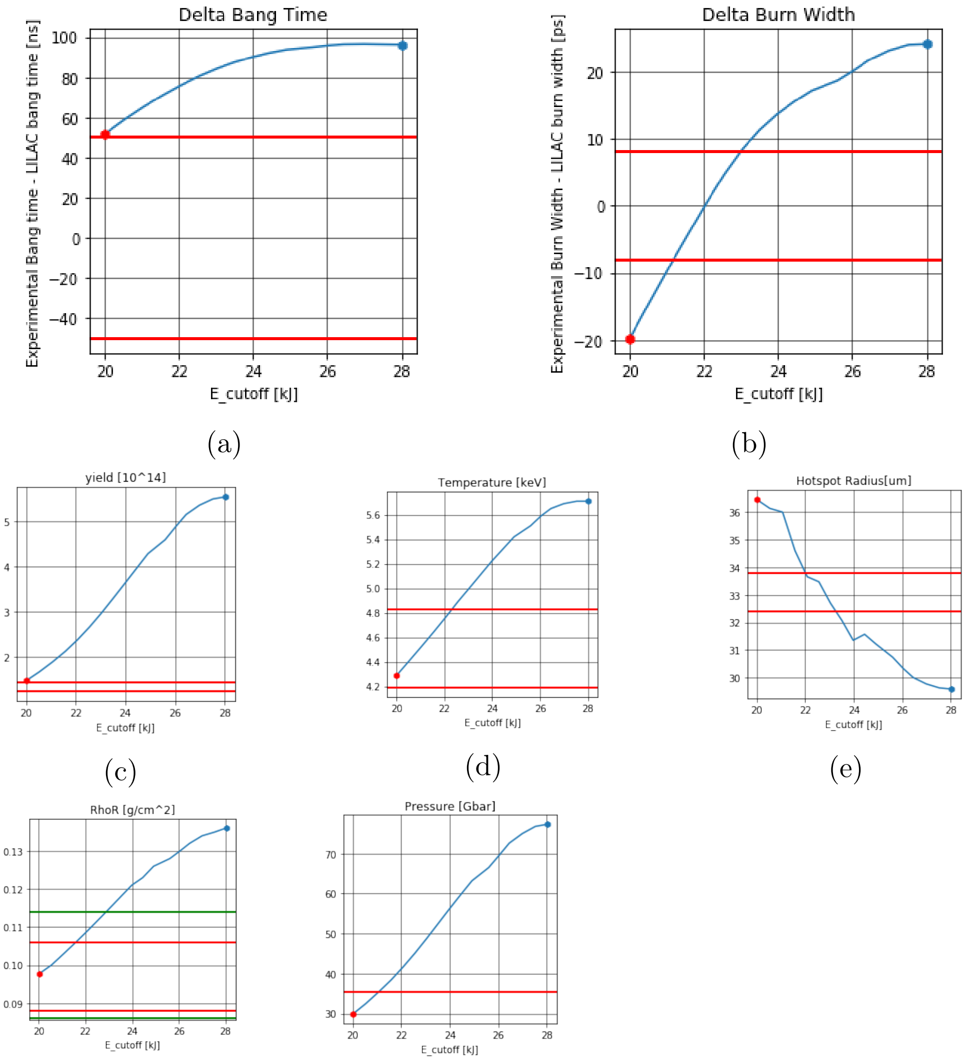

(a) (b)

(c) (d) (e)

(f) (g)

Figure 3.2: Variation in the observables caused by modifications of the laser of type 1 for 87266, plotted as functions of E_{cutoff}; the first two plots, namely fig. 3.2a and 3.2b, are the curves for bang time deltas and burn width deltas. The following plots are, in order, the curves representing the degradations trends of yield, temperature, radii, areal densities, and lastly pressures. As previously stated, for degradations of type 1, the x axis corresponds to the values E_{cutoff}. Each point in the blue curves corresponds to observables from different LILAC simulations. The red points represent the values for the observables of the selected simulation, and the two red lines present in each plot give the range provided by the experimental measurement. It should be noted that for the case of the pressure, no straightforward error bars were available, therefore in figure 3.2g there is only one red line, the one corresponding to the inferred pressure.

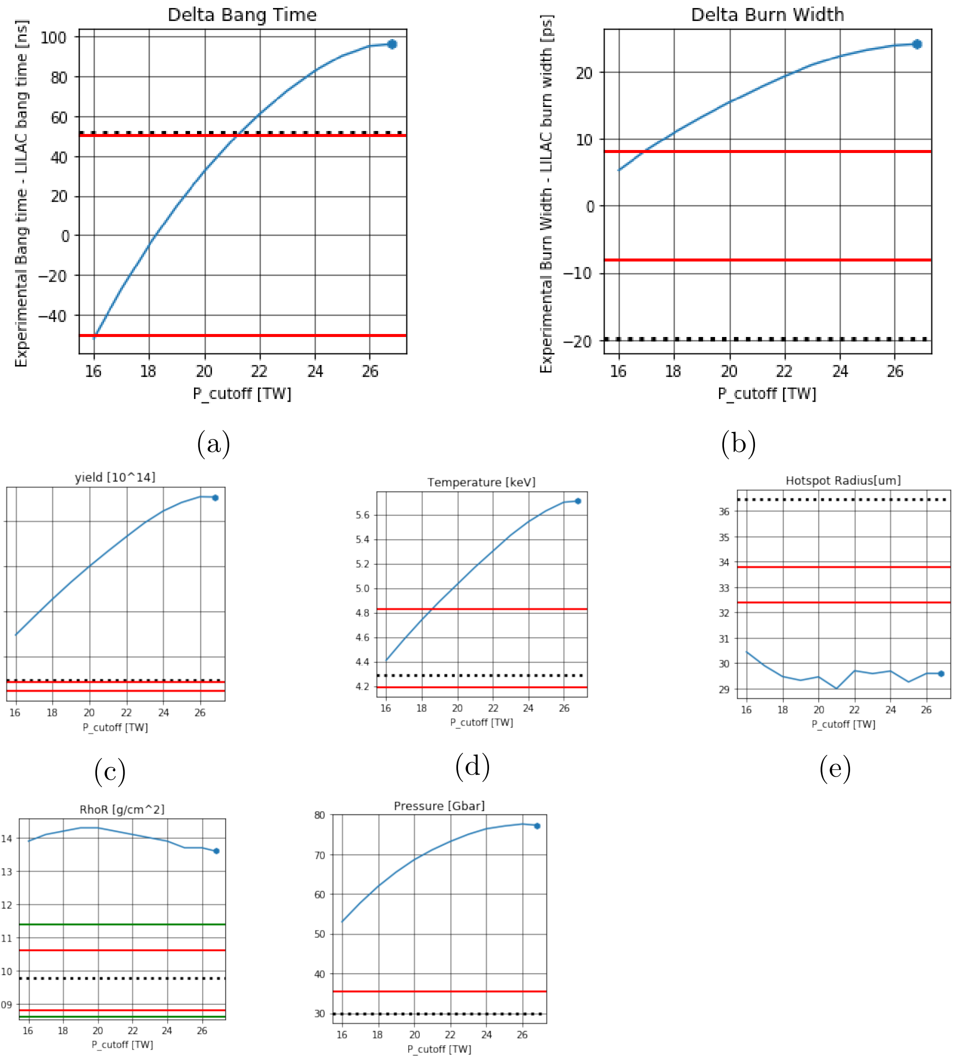

(a) (b)

(c) (d) (e)

(f) (g)

Figure 3.3: Variation in the observables caused by modifications of the laser of type 2 for 87266, plotted as functions of P_{cutoff}; the first two plots, namely fig. 3.2a and 3.2b, are the curves for bang time deltas and burn width deltas. The following plots are, in order, the curves representing the degradations trends of yield, temperature, radii, areal densities, and lastly pressures. As previously stated, for degradations of type 2, the x axis corresponds to the values of P_{cutoff}. Each point in the blue curves corresponds to observables from different LILAC simulations. The black dashed lines correspond to the values of the observables for the selected simulation, and the two red lines present in each plot give the range provided by the experimental measurement. It should be noted that for the case of the pressure, no straightforward error bars were available, therefore in figure 3.3g there is only one red line, the one corresponding to the inferred pressure.

changes of type 2 that cause a similar shift in bangtime, cause an increase in burn width of only about 10 ps. Similar considerations can be made for 88314.

On the grounds of plots (a) and (b) in figures 3.2 through 3.5, the following considerations can be made:

- for 87266: perturbations of type 2 seem to favored, as they offer bang times and burn width in the range of the experimental measurements, but at the cost of a heavy change in the laser pulse shape, that is by reaching values of P_{cutoff} of about 16 TW of peak laser power; figures 3.2a, 3.2b seem to suggest that it's not possible to match both bang time and burn width for modifications of type 1. It should be kept in mind that 2-D perturbations can cause slight changes to bang times and burn width.
- for 88314: since the clean LILAC bang time is already within the error bar, simulations causing it to shift outside of the experimental range are not desirable, and this sets a lower limit to the range of possible perturbations to 20 kJ for E_{cutoff} and to 20 TW for P_{cutoff}. In these ranges, only modifications of type 1 can match the experimental bang time, and therefore they seem to be the most likely candidate. In particular, simulations with E_{cutoff} between 20 and 22 kJ seem to be the most favored, as they have burn widths that are in the experimental range.

These considerations provide a first step towards finding the perturbations that best suit the two experiments, but are far from the complete picture; these considerations suggest that there are multiple simulations that could provide the experimental values, but considerations based on the plots for the other observables provide a useful tool for reducing this freedom. Therefore the candidate now proceeds to compare the remaining observables. These are shown in plots (c) through (g) in figures 3.2 through 3.5. Different considerations can be made regarding these plots for 87266 and for 88314.

Regarding 87266, figures 3.3c through 3.3g show that yield, areal density, hotspot radius, and pressure don't match the experimental results well. In addition, a comparison with plots 3.2c through 3.2g shows that of the above mentioned observables, yield, areal density and pressure are better matched by simulations of type 1. In light of these considerations a riexamination of the choice made on the grounds of considerations concerning the bang times

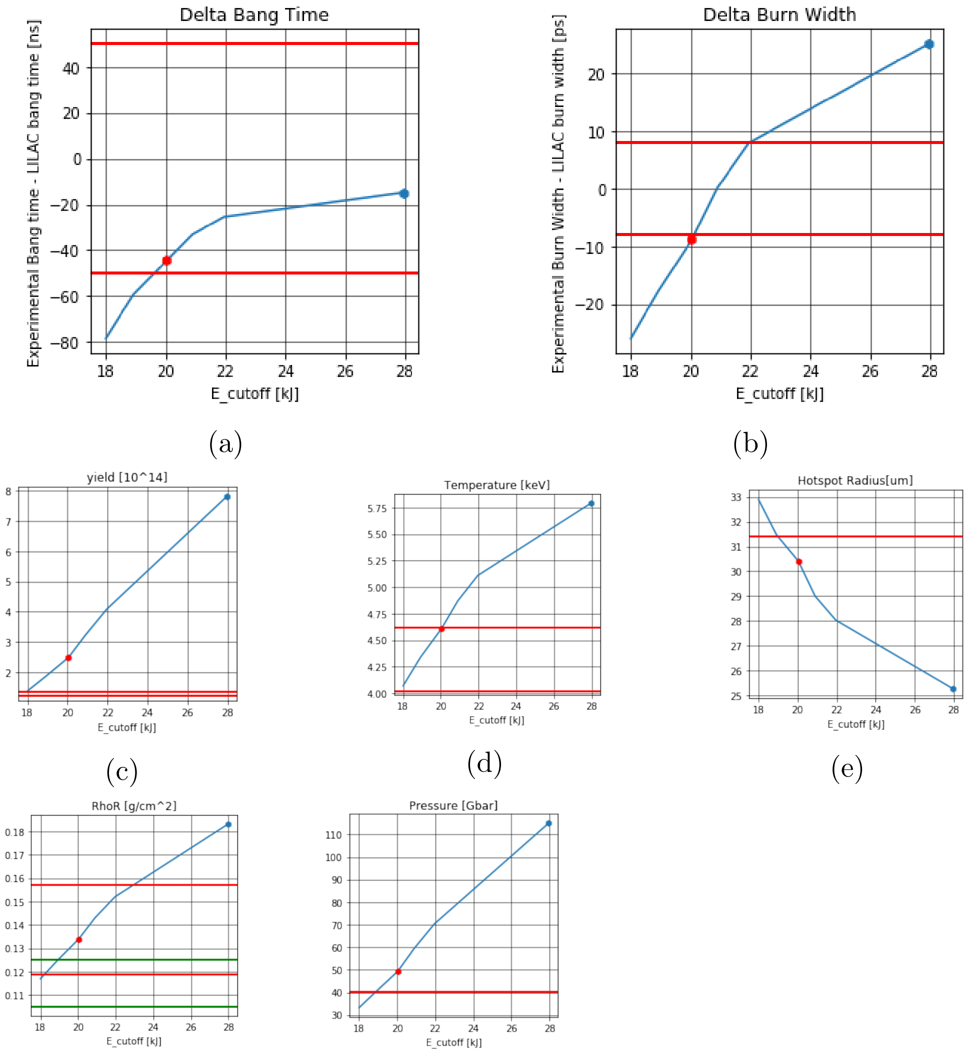

(a) (b)

(c) (d) (e)

(f) (g)

Figure 3.4: Variation in the observables caused by modifications of the laser of type 1 for 88314, plotted as functions of E_{cutoff}; the first two plots, namely fig. 3.4a and 3.4b, are the curves for bang time deltas and burn width deltas. The following plots are, in order, the curves representing the degradations trends of yield, temperature, radii, areal densities, and lastly pressures. As previously stated, for degradations of type 1, the x axis corresponds to the values of E_{cutoff}. Each point in the blue curves corresponds to observables from different LILAC simulations. The red points represent the values of the observables for the selected simulation, and the two red lines present in each plot give the range provided by the experimental measurement. It should be noted that for the case of the pressure, no straightforward error bars were available, therefore in figure 3.4g there is only one red line, the one corresponding to the inferred pressure.

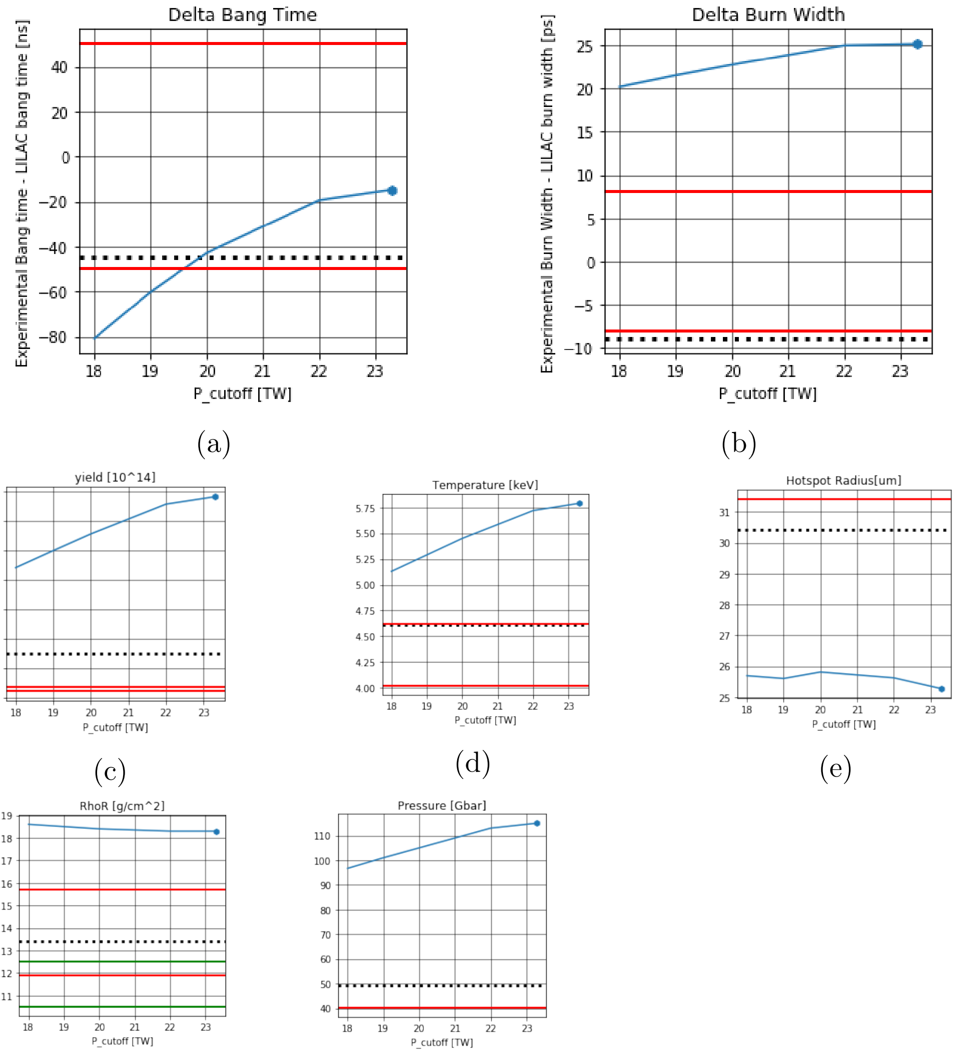

(a) (b)

(c) (d) (e)

(f) (g)

Figure 3.5: Variation in the observables caused by modifications of the laser of type 2 for 87266, plotted as functions of E_{cutoff}; the first two plots, namely fig. 3.4a and 3.4b, are the curves for bang time deltas and burn width deltas. The following plots are, in order, the curves representing the degradations trends of yield, temperature, radii, areal densities, and lastly pressures. As previously stated, for degradations of type 2, the x axis corresponds to the values of E_{cutoff}. Each point in the blue curves corresponds to observables from different LILAC simulations. The black dashed lines correspond to the values of the observables for the selected simulation, and the two red lines present in each plot give the range provided by the experimental measurement. It should be noted that for the case of the pressure, no straightforward error bars were available, therefore in figure 3.5g there is only one red line, the one corresponding to the inferred pressure.

and burn widths is in order. While it is true that bang times and burn widths are matched best by perturbations of type 2 at P_{cutoff} of about 16 TW, the significantly better match with experiment provided by the simulation with laser energy of 20 kJ suggest it as the best choice for the 1-D degradation of 87266, leaving the task of matching the bang times and burn widths to a 2-D degradation mechanism. An additional reason for this choice is that a P_cutoff of 16 TW is a significant reduction from the $\sim$ 27 TW of the original laser pulse; while it may be possible to obtain the experimental results by further degrading (in 2-D) these already heavily perturbed implosions, the necessary 2-D perturbations would be significant, possibly leading to a very different implosion compared to the original one.

For 88314 the analysis is more straightforward because the simulations that seemed promising in figures 3.4a and 3.4b are the most promising ones also in plots 3.4c through 3.4g. While in these last plots the points corresponding to the best match with experiments is 18 kJ, the limitation within the range 20-22 kJ found when considering the bang times caused the selected simulation to be the one with a E_{cutoff} of 20 kJ. Furthermore, even a brief look at plots 3.5c through 3.5g clearly shows that, in the plotted range, all observables are further from the experimental values than the simulation of type 1 at 20 kJ of laser energy. If one assumes the plotted trends also for lower powers, it is likely for some of the observables to reach values closer to exeperiment, in particular yield, temperature, and pressure, but the other time integrated observables seem to be weakly dependent on P_{cutoff}r. In addition, when extrapolating the likely behavior of simulations with lower P_{cutoff}, plots 3.5a and 3.5b suggest that, while it may be possible to match the burn width, it is highly unlikely to be able to also match the bang time, which would be unnecessarily postponed.

Modifications of the lasers of type 3 are not shown in this chapter for the sake of brevity. Because of their dependence on both E_{cutoff} and P_{cutoff}, it was necessary to analyze a plethora of plots[27] whose presence here would only serve to render the current section monotonous and interminable.

Fortunately, all of the plots analyzed related to degradations of type 3 led to the same conclusions, and there was no evidence that analyzing a more ample range of values for E_{cutoff} and P_{cutoff} would lead to better results. Considerations analogous to the ones above were done on many possible combinations, for both 87266 and 88314; the conclusions reached were that none of them provided better matches with experiment than the perturbations of type 1 selected; some of the trends found even suggested that the ideal degradations are the ones selected above.

In conclusion, after a thorough study of the possible 1-D degradation mechanisms and after having found simulations to minimize the differences between simulations and experiment, in order to have a closer match to experiment it is still desirable:

- for 87266: to slightly reduce yield, hotspot radius, and burn width and to delay the bang time
- for 88314: to reduce the yield and possibly the pressure

3.4 2-D Reconstruction of the Implosion Core

In this section the candidate proceeds to illustrate the 2-D degradation mechanisms studied for the shots examined, after a brief introduction to the code used for the 2-D simulations.

The code used in this section is DEC2D. This is a two-dimensional radiation hydrodynamics code, which uses a MacCormack scheme. The code assumes cylindrical symmetry, and therefore allows only two-dimensional perturbations. It is used to simulate the deceleration phase of the implosion and the effect of asymmetries on implosion quantities, such as neutron averaged quantities and x-ray data. It relies on modeling a single mterial, made of 50% deuterium and 50% tritium. In order to account for the fact that the composition in the shell (the main contributor to the mass of the target) for 87266 and 88314 was 60/40 (60% tritium), a few small modifications were made to the code in order to account for the average particle density, which in turn affected the hydrodynamics, and the reduction in the cross section; this last aspect depends on the fact that with 50/50 composition, the product of the densities can be written as $\frac{n^2}{4}$, whereas in the case of 60/40 composition this product becomes $\frac{6}{25}n^2$. The code does not include a model for laser drive, therefore, in order to obtain results for an implosion simulation, it is necessary to rely on the 1-D code LILAC used for the purposes of section **??** using the following steps:

- the desired implosion is simulated in LILAC
- the time for the start of the deceleration phase is selected, by finding the moment in the LILAC simulation when the return shock hits the shell. This time, in most implosions, coincides with the time when the

laser is shut off. This time corresponds with the initial time for the DEC2D simulation.

- the profiles at the selected time are imported into DEC2D as initial conditions.

Apart from the first item in this list, all other steps were completed in an automated fashion using the Python code written by the author and illustrated in appendix A. The code has a wide applicability as it can provide the time corresponding to the start of the deceleration phase for most shots in the database of LILAC simulations for cryogenic implosions . In addition to finding the time step, it also generates the text file containing the profiles for radius,density, pressure, velocity, electron and ion temperature as a function of radius at the selected time.

The code also requires an input deck, containing all the preferences for the settings of the code; the ones that, for the purpose of this thesis, most often changed from simulation to simulation are:

- the final time for the simulation; the simulation needs to run for long enough to capture the entire neutron rate. When neutron production stops, the neutron averaged values no longer change.

- the alpha particle deposition (i.e. alpha heating) is turned off depending on the requirement. On Omega targets, the production of alpha particles is so small that their presence doesn't affect the implosion, and therefore after their production, they are treated as if they had left the system. On NIF scale, the presence or absence of alpha heating can significantly affect the implosion, and therefore simulations on NIF are run with both options for alpha heating.

- the radius of cutoff; this is the radius of the DEC2D domain. It is usually selected as 1.4 to 1.8 times the radius at maximum density. For the NIF scale simulations with alpha deposition, it is often necessary to use a bigger radius of cutoff in order to have the simulation converge.

- the radius where the perturbation is to be introduced and the type of perturbation to be introduced; in particular single or multi-mode, and if multi-mode, which combination and, in addition, the amplitude of the perturbation.

Table 3.5: Comparison between the $E_{cutoff} = 20$ kJ simulations in LILAC and DEC2D for 87266 and 88314, part I. The experimental results are also present for convenience. Note that the radii from LILAC are not exactly the ones present in the plots in section 3.3, as the ones in this table have been calculated using SPECT3D.

Shot Number	**Ion Temperature** [keV]	**Hotspot Radius** [μm]	**Areal Density**[mg/cm^2]	
87266, Exp.	4.51 ± 0.32	33.1 ± 0.7	97 ± 9	100 ± 14
87266, LILAC	4.29	31.7	98	
87266, DEC2D	4.10	32.0	110	109
88314, Exp.	4.32 ± 0.30	31.4	115 ± 10	138 ± 19
88314, LILAC	4.61	27.5	134	
88314, DEC2D	4.45	27.5	151	147

Table 3.6: Comparison between the $E_{cutoff} = 20$ kJ simulation in LILAC and DEC2D for 87266 and 88314, part II. The experimental results are also present for convenience. Note that the radii from LILAC are not exactly the ones present in the plots in section 3.3, as the ones in this table have been calculated using SPECT3D.

Shot Number	**Yield** [10^{14}]	**Pressure** [Gbar]	**Burn Width** [ps]	**Bang Time** [ns]
87266, Exp.	1.34 ± 0.1	35.5	81 ± 8	2.193 ± 0.05
87266, LILAC	1.47	37.53	101	2.141
87266, DEC2D	1.62	43.7	87	2.151
88314, Exp.	1.28 ± 0.06	40.2	78 ± 8	2.155 ± 0.05
88314, LILAC	2.48	60.83	87	2.200
88314, DEC2D	2.81	72.55	74	2.202

- settings related to the output of data necessary for the analysis of the implosion (IRIS3D, SPECT3D, the codes used to obtain more accurate estimates of, respectively, the areal density and the radius)

Tables 3.5 and 3.6 show the results of the clean 20 kJ simulation compared to the LILAC results. The results are close, but not exact. This is due to differences between the two codes, or to differences in the models used in the two codes. Since further degradations are necessary for both 87266 and 88314 no tuning of the DEC2D code to match the LILAC results was necessary.

Perturbations are introduced via changes in velocity at the time chosen as the start of the deceleration phase and at the radius where the shell reaches the $1/e$ point, inside the shell. This perturbation in velocity, within the first tens of picoseconds, propagates to the other hydrodynamic quantities. Modes are classified based on the wavelength of the perturbation. The mode number consist in the ratio of the wavelength of the perturbation to the circumference of the shell. Modes between 2 and 6 are considered "low modes", modes between 8 and 40 are "mid modes". As explained in chapter 2.5 high modes grow much less than low and mid modes, as they have smaller linear growth rates, and modes with $l > 90$ are exponentially decaying in time. Only even integer modes are considered, because simulations with even wavelengths can be simulated without loss of information in a single R-Z quadrant, given the symmetry with respect to both the R and the Z axis. Odd numbers would require to perform the simulation over two quadrants.

The data shown in tables 3.5 and 3.6 is the starting point for the 2-D degradation of the implosion. The main differences left between simulations and experimental results are different for 87266 and 88314, and lead to different conclusions regarding the spectrum of the mode.

For 87266, the most important differences between the simulation and experiment are that the bang time is still slightly earlier than the experimental value and that the pressure and yield are higher than their experimental counterparts. Simulations were run with different amplitudes of mode 2 and mode 10, in order to establish if low or mid modes were more likely to explain the remaining differences. Figure 3.6 shows these trends, as a function of the degradation in yield. The red lines provide the acceptable experimental ranges. Since a very small degradation in yield is necessary, both degradations could explain most of the observables. The choice of a mode two degradation was informed mostly by the radius and pressure plots, in which it's clear that a mode 2 degradation would match experiment best. The final comparison with experimental results is discussed in 3.5; the data related to the final degradation chosen for 87266 can be found in table 3.7.

The biggest difference for the case of 88314 is that a much higher degradation in yield is necessary, and therefore the differences between the different possible mode spectrums become more significant. In addition, all other observables, with the exception of the radius the match experiment closely. This was the same for the shots described in ref. [7]; therefore a similar approach to the one used in ref. [7] was pursued. The chosen spectrum consisted in a 5 % mode 2 perturbation, in addition to a flat spectrum up to mode 20 and a $1/l^2$ decay for modes with $l > 20$ of amplitude 2%. For the purposes of reconstructing 88314, various simulations were performed. The variables considered in this process were the ratio between the amplitudes of mode two and of the rest of the spectrum (r), and a multiplier to increase or decrease the overall amplitude of the spectrum (m). The ranges of values used for r and m were, between $\frac{1}{5}$ and 1, and between 0 and 25%, respectively. Not all of these simulations converged; for simulations with high values of r, the

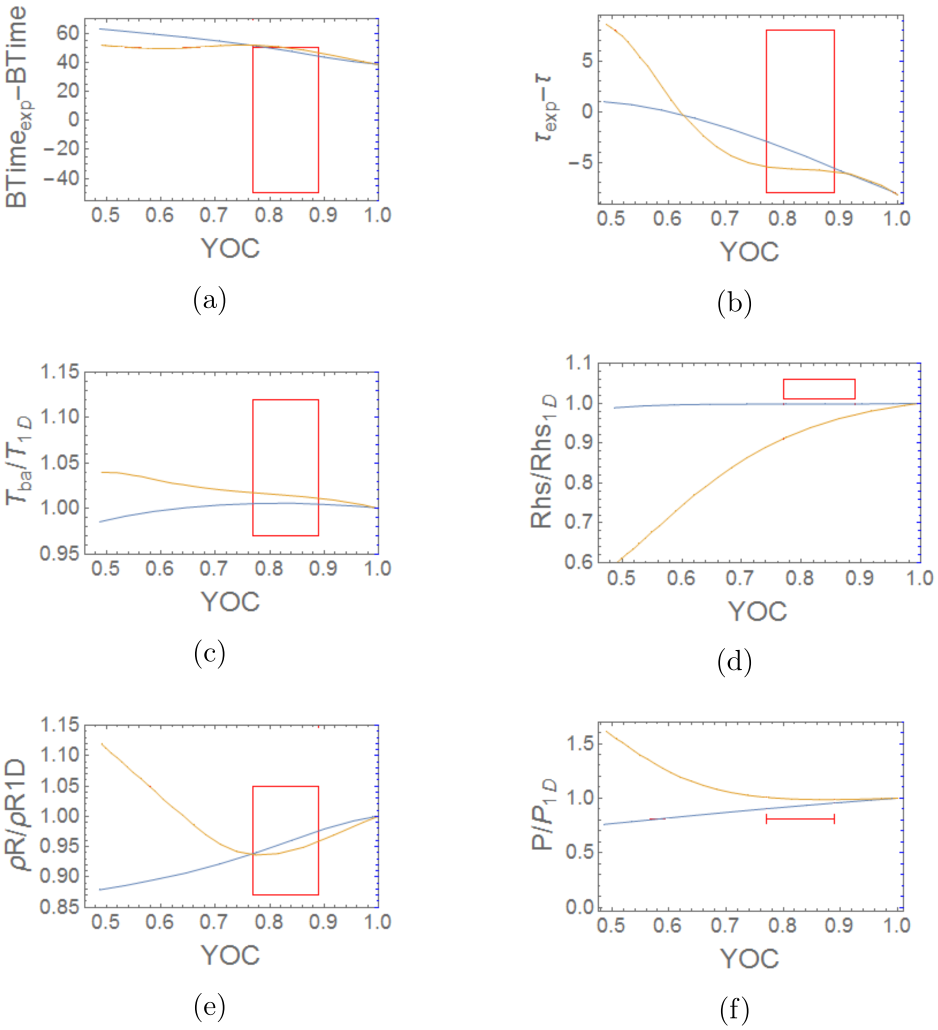

Figure 3.6: Trends caused by mode two degradations (in blue) and by mode 10(in orange) for 87266. YOC stand for "yield over clean", and is the ratio between the yield and the yield with no degradation. The red lines provide the range of acceptable values, and are based on the experimental measurements, plus or minus the error.

upper limit for m was lower than 25% because simulations with high values of both r and m are very heavily perturbed and are likely not to converge. A similar study to the one done with LILAC and described in 3.3 was then conducted. The best match with experiment that was found to be with $r = 2$ and $m = 2.2$. In addition, simulations were run for mode 2 and for for the flat+$1/l^2$ perturbations. These are shown in figure 3.7. These are useful to see which of the two combined spectra (mode 2 or flat+$1/l^2$) play a more important role in implosion number 88314.

It should be noted that an effort was made to find a way to calculate the radii using only the DEC2D simulation. For all the simulations mentioned in this thesis it was necessary to run an additional simulation in SPECT3D to obtain a more accurate estimate of the radius. SPECT3D is a multi-dimensional collisional-radiative spectral analysis code designed to simulate the atomic and radiative properties of laboratory and astrophysical plasmas. The forementioned effort had a twofold objective: most importantly, it allowed to have estimates of the radii for NIF scale simulations. SPECT3D requires the response function of a given detector, and this data was not available for NIF. Secondly it should be noted that the SPECT3D simulations for 2D codes are very time consuming; while a DEC2D simulation with standard resolution (about 400 by 400 grid points) required 4 hours to run, the corresponding SPECT3D simulation would take at least twice that time, and required DEC2D to output additional and very large amounts of data. The ability to obtain an estimate of the SPECT3D radius running a single DEC2D simulation cannot be overstated.

In order to achieve the goal of obtaining reasonable estimates for the "SPECT3D values" of the radii, the following was done, following the example in ref. [7]: Starting from the formula to obtain a neutron averaged volume, obtained by simply using 1 as the Q in 3.1, a new "burn volume", V_a is defined in the following way:

$$V_a = \frac{\int dt (\int dV (n_D n_T \langle \sigma v \rangle)^a)^2}{\int dt \int dV (n_D n_T \langle \sigma v \rangle)^{2a}} \tag{3.2}$$

In this new definition, a is a weight assigned to the number of fusion reactions per unit volume and per unit time. Higher values of a provided smaller hotspot volumes, giving estimates of the radius of the inner neutron producing region, while smaller values of a provide good estimates for the volume included within the bubbles.

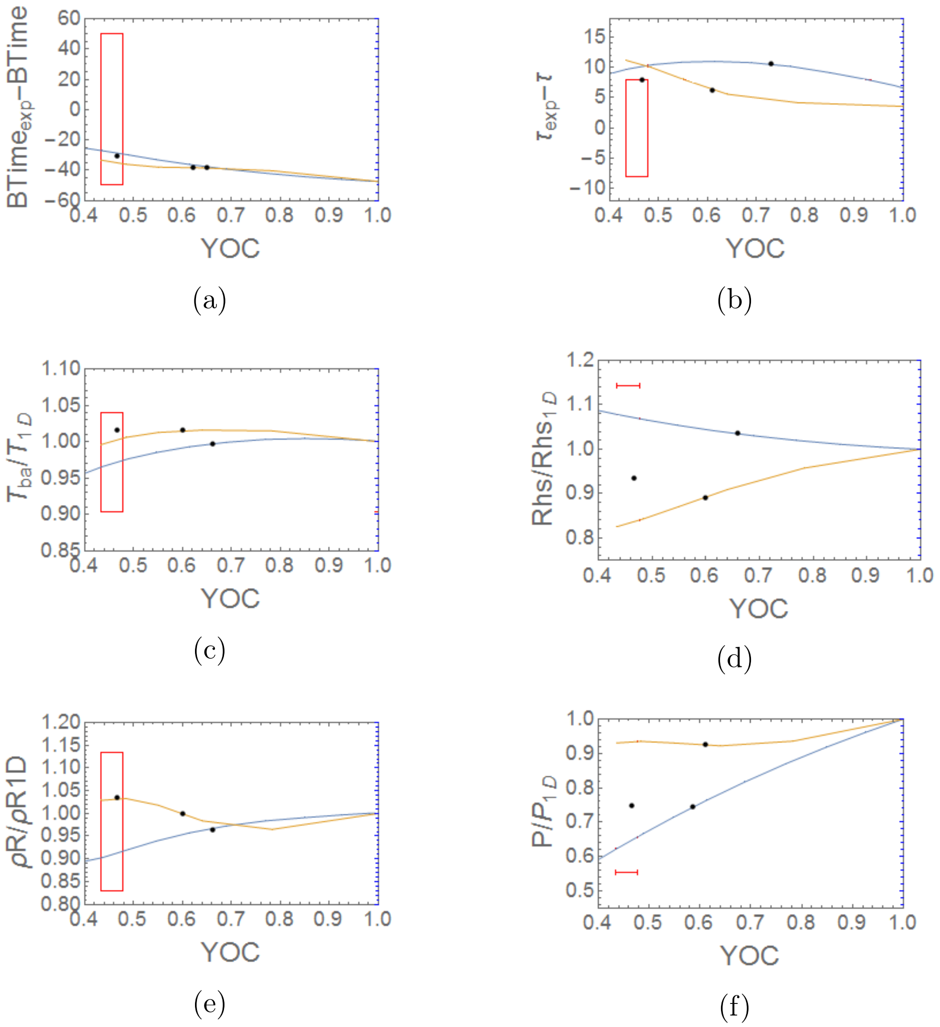

Figure 3.7: Trends caused by mode two degradations (in blue) and by a flat spectrum from mode 4 to 20 with a $1/l^2$ decay for modes higher than 20 (in orange) for 88314. YOC stand for "yield over clean", and is the ratio between the yield and the yield with no degradation. The red lines provide the ranges of acceptable values, and are based on the experimental measurements, plus or minus the error. The dots on the curves correspond to the final value selected for that type of perturbation. The third point is the point corresponding to the 2-D degraded simulation, with a combination of the two types of degradation.

The DEC2D source code was then modified in order to allow for the output of V_a for different values of a. The code already outputted V_a with $a = 1$ and $a = 0.5$, and it was found that the SPECT3D values were always in the middle of these two extremes. Therefore, the code was modified in order to allow the output of values of a between 0.6 and 0.9. The closest match with the SPECT3D values was provided by a=0.7 for the case of 88314, and was provided by 0.5 for the case of 87266.

In summary, in this section the radiation hydrodynamics code DEC2D was briefly introduced, together with a quick guide. The code was then used in order to find the most likely 2-D degradations that could explain the eperimental results. These were found, and resulted in a fairly close match with experiment, illustrated in tables 3.7 and 3.8. Lastly, a brief description of how to obtain estimates for the "SPECT3D" value of the radii and the advantages of such a method were illustrated. This step was necessary in order to obtain realistic estimates for the radii on NIF scale implosions in the next chapter.

3.5 Final Comparison With Experiment

The final comparisons between the experimental values and the chosen 1- and 2-D perturbed simulations are shown in tables 3.7 and 3.8. It should be noted that there are some remaining differences, meaning that there could be mechanisms in action that can't be described by a hydrodynamically pertrubed implosion. These differences are different for 87266 and for 88314.

For 87266, the temperature and hotspot radius are somewhat smaller than the experimental value, while the pressure is slightly higher than in experiment. It should be noted that the pressure has a strong dependence on the radius, and therefore the "real" differences are only the neutron averaged ion temperature and the hotspot radius. In addition, being an inferred quantity, there is no straightforward way to compute the error on the experimental pressure, and, as a consequence, the lack of an exact match between computation and experiment for pressure is not as important as for other experimental observables, that are directly measured, and have estimates for their error bars.

For 88314 the only significant differences are the radius and the pressure. The previously mentioned strong dependence of the pressure on the radius would cause the estimate of the pressure to decrease to values much closer to

Table 3.7: Comparison between the 20 kJ simulations in LILAC and DEC2D for 87266 and 88314, part I. The experimental results are also present to make the comparison easier. Note that the radii from LILAC are not exactly the ones present in the plots in section 3.3, as the ones in this table have been calculated using SPECT3D. Comp. stands for "computed"

Shot Number	**Ion Temperature** [keV]	**Hotspot Radius** [μm]	**Areal Density**[mg/cm^2]	
87266, Exp.	4.51 ± 0.32	33.1 ± 0.7	97 ± 9	100 ± 14
87266, Comp.	4.04	31.1	105	101
88314, Exp.	4.32 ± 0.30	31.4	115 ± 10	138 ± 19
88314, Comp.	4.52	25.3	137	133

Table 3.8: Comparison between the 20 kJ simulation in LILAC and DEC2D, part II. The experimental results are also present to make the comparison easier. Note that the radii from LILAC are not exactly the ones present in the plots in section 3.3, as the ones in this table have been calculated using SPECT3D.

Shot Number	**Yield** [10^{14}]	**Pressure** [Gbar]	**Burn Width** [ps]	**Bang Time** [ns]
87266, Exp.	1.34 ± 0.1	35.5	81 ± 8	2.193 ± 0.05
87266, Comp.	1.34	42.2	87	2.151
88314, Exp.	1.28 ± 0.06	40.2	78 ± 8	2.155 ± 0.05
88314, Comp.	1.31	56.9	70	2.185

the experimental pressure for an increase from 25.3 to 30 μm in the computed radius. All other observables are within the error bar of the experimental values.

Chapter 4

Hydrodynamically Equivalent Scaling of the Implosion Core

4.1 Introduction

In this chapter the goal of the thesis is reached, namely an extrapolation of low-converging cryogenic Omega implosions to spherically symmetric direct drive NIF energies of 1.9-2.5 MJ. The choice of the range of energies was determined by the fact that currently the NIF is capable of delivering up to $\sim$ 2.5 MJ of energy on target at full capacity, but has currently delivered a maximum of $\sim$1.9 MJ. Therefore the two extremes of the interval 1.9 - 2.5 were chosen, with the addition of 2.0 MJ as an intermediate value. The current laser configuration consists of 192 beams in a polar geometry: this means there are no laser beams in the equatorial region and that the laser cannot be used for spherically-symmetric implosion experiments. As a consequence, it is being used in polar-direct-drive[30] (PDD) mode to test direct drive. PDD is expected to achieve lower performance levels than symmetric drive. Considering the fact that spherically symmetric direct drive experiments are routinely being conducted on the OMEGA laser and the fact that shots on OMEGA are more cost effective than shots on NIF, the capability of extrapolating OMEGA results to NIF scale presents itself as an incredibly valuable tool for research in direct drive ICF.

The fusion yield for the cores reconstructed in chapter 3 is estimated to be between $\sim$ 220 and 260 kJ when upscaled to 1.9 MJ NIF, while for the 2.5 MJ it is estimated to be between 350 and 410 kJ. The level of alpha heating and yield ampli

cation for the 1.9 extrapolations is predicted to be similar to that achieved with the 1.9 MJ indirect-drive NIF high foot (HF) implosions[19]. The HF implosions have achieved record fusion yields of nearly 10^{16} neutrons or about 26 kJ of fusion energy[20,15], demonstrating significant levels of alpha heating. Based on analytic models and numerical simulations[3,13], it was estimated that alpha-particle heating has led to $\sim 2-2.5$x increase in the fusion yield[3,20,15]. In the absence of alpha heating, the fusion yield from hydrodynamic compression alone would have been $\sim 4-5*10^{15}$. By extrapolating recent OMEGA results in size to match the 1.9 MJ of incident NIF laser energy, it is found that the best performing direct-drive OMEGA implosions to date would lead to neutron yields of the order of 10^{17} neutrons and a level of alpha heating corresponding to about 1.8 - 2.0 yield enhancement, only somewhat smaller than the indirect-drive HF targets at the same laser energy. The larger fusion yield in direct drive, results from the larger size and fuel mass of the 1.9 MJ direct-drive targets.

In this chapter the techinque for the upscaling of Omega implosions to NIF sizes is illustrated and used in order to obtain quantitative predictions; the necessary theoretical considerations and results are introduced in section 4.2. In more detail, the purpose of 4.2 is threefold: first the main results from the analytic theory of the three-dimensional hydro-equivalent scaling developed by Nora et al.[28] and Bose et al.[10] are illustrated. These theories do not include the effect of alpha heating and can only be applied to extrapolate fusion yields and hydrodynamic properties due to compression alone without accounting for alpha-energy deposition (i.e. "no-alpha" properties). Therefore, subsequently, some results from the model by Betti et al.[3], are shown, in order to estimated the fusion yield via the "no-alpha" properties of the implosion. Lastly, these results are applied to the shots examined for the purpose of this thesis, namely 87266 and 88314.

Subsequently, in section 4.3, the process of obtaining numerical estimates for the extrapolation is illustrated, and the results from the 2-D simulations are shown, in order to validate the theoretical predictions. This last step is done section **??**; in this context it is found that the predictions are in fairly good agreement with the values from simulation.

Finally, section 4.4 provides final considerations regarding the current and the previous chapter; the steps necessary to obtain analytical and numerical estimases for NIF-scale symmetric direct drive implosion are reviewed.

4.2 Theory

In this section, the main results from the theory of hydrodynamic equivalence[28,10] are illustrated, in order to obtain estimates for the performance of OMEGA shots on more energetic laser facilities. This method provides estimates of the effect of compression alone and does not account for the contribution due to alpha heating. While the effect of alpha heating is small for laser facilities of the size of the OMEGA laser, this is not the case for larger facilities, where the presence of alpha heating can play an important role. For this reason, subsequently, the main results from the theory developed by Betti et al. in ref.[3] are provided. Lastly thse results are applied to the cases of 87266 and 88314.

With regard to laser plasma instabilities and interactions (LPIs) in the coronal plasma, it is important to point out that this thesis work does not attempt to estimate the scaling of LPIs. LPIs do not scale proportionally with size and it is therefore not possible to quantitatively extrapolate the effects of LPIs at NIF energies from OMEGA results. LPI experiments at ignition scale energies on the NIF will be conducted over the next several years to determine laser-target coupling and the effects of LPIs. The goal of these studies is to demonstrate coupling similar to or improved over that observed on OMEGA. For the purpose of the hydrodynamic equivalence extrapolation model, we assume that LPIs on NIF will allow to reproduce the same OMEGA implosion (equal velocity and adiabat) at the larger scale to match the 1.9-2.5 MJ NIF energy. Additionally, predicting the performance on different laser systems (OMEGA and NIF) is also not the purpose of this thesis. Such an extrapolation depends on the ability to correctly simulate current and future experiments, and to correctly capture all the sources of degradation[18] of implosion performance from low- to high-mode asymmetries, from nonlocal electron transport to laser plasma coupling. The goal of this chapter is not quite as ambitious but much more robust since it only assumes that the core conditions of an OMEGA implosion can be identically reproduced (same pressure, shell density, and shape) but with a larger spatial size on a larger laser facility. Therefore, in terms of hydrodynamic performance, the implosions at 1.9 MJ are assumed to be identical to the OMEGA implosions, just larger in target size by a factor of $(E_{NIF}/E_{\Omega})^{1/3}$.

The theory of hydrodynamic equivalence provides a way to extrapolate implosion performance on the OMEGA laser system to higher scales. In the precursor to the current work[7] it was shown that the implosion hydrodynamics are determined by the internal energy of the hot-spot at stagnation,

$$P_h V_h/(\Gamma - 1), \tag{4.1}$$

where P_h and V_h are the stagnation pressure and volume, where stagnation is defined as the moment of maximum contraction of the target. As a consequence of this, in the theory of hydro-equivalent scaling P_h is kept constant, causing the hydrodynamics to be scale independent. In order to obtain a scale invariant pressure some limitations of the other parameters characterizing an implosion are necessary, in particular[28]:

- equal values of the implosion velocity V_{imp}, shell adiabat α_0, and laser intensity I_L are required.
- the initial seeds of the instability must scale proportionally to the target radius R
- it is necessary for the target dimensions (i.e. radius R and shell thickness Δ and time scale with laser energy E_L as

  $$R \sim \Delta \sim E_L^{1/3}; t \sim R \sim E_L^{1/3}, \tag{4.2}$$

  where $E_{L_{NIF}}/E_{L_\Omega} \approx 4.08^3$, for the 1.9 MJ case.

As a consequence of this last consideration target sizes and laser pulse shapes for extrapolated direct-drive (NIF) ignition-scale implosions are four times larger and longer than on OMEGA. Ref. [28] shows that if all these criteria are met the acceleration-phase RTI also scales hydro-equivalently.

Unlike the pressure, the implosion yield (no-α) is not a scale invariant quantity because

$$Y \sim P_n^2 T_n^{1.7} \tau_n V_n \tag{4.3}$$

is determined by the scaling of the temperature T_n , which depends on the scaling of hot-spot transport properties (i.e., thermal and radiation transport). This dependence can easily be shown, considering that the reaction rate is proportional to $n^2\langle\sigma v\rangle$ and therefore the yield can be calculated in the folloing way:

$$Y \sim n^2 \langle\sigma v\rangle V\tau, \tag{4.4}$$

where V is the neutron producing volume and τ is the time of neutron production. In addition, treating the core as an ideal gas, n follows $n \sim \frac{P_n}{T_n}$.

Lastly, in the range 2 keV $< T <$ 7keV,

$$\frac{\langle \sigma v \rangle}{T_n^2} \sim T_n^{1.7}. \tag{4.5}$$

If all of these considerations are substituted into equation 4.4, equation 4.3 is obtained. It was shown by Bose in ref. [7] that, in the case of hydro-equivalent scaling, the temperature scales as $T \sim E_L^{0.06} \sim R^{0.18}$. Assuming that $V \sim R^3 \sim E_L$ and $\tau \sim R \sim E_L^{1/3}$, equation 4.3 reduces to

$$Y_{no-\alpha} \sim R^{4.3} \sim E_L^{1.43}. \tag{4.6}$$

In addition to the Rayleigh-Taylor (RT) unstable outer surface during the acceleration phase, the inner surface of the shell is also unstable to the RTI during the deceleration phase. The RT spikes stream into the hot spot, causing a decrease in the stagnation pressure or the burn volume and increasing the surface-to-volume ratio of the hot spot. This in turn increases the conduction losses[24], resulting in a reduction in hot-spot temperature. The perturbations rapidly become nonlinear, and a significant fraction of the shell's kinetic energy is used to feed lateral motion, instead of contributing to the hot-spot pressure through radial compression[25,34]. The effective areal density ρ R of the shell is expected to decrease and degrade the confinement time, hot-spot pressure, and neutron yield. The yield-over-clean (YOC or Y/Y_{1-D}) is used as a measure of the effect of hydrodynamic instabilities on the implosion performance[12]:

$$YOC = \Big(\frac{\text{yield from experiments or 2- or 3-D similations}}{\text{yield from 1-D simulation}}\Big) \tag{4.7}$$

We now consider the hydrodynamic scaling of the deceleration-phase RTI[9]. The growth rate for the instability in the linear regime can be approximated with[37]

$$\gamma_{RT} = \alpha \sqrt{\frac{k\langle g\rangle}{1 + k\langle L_{min}\rangle}} - \beta\langle V_{abl}\rangle \tag{4.8}$$

where $\langle g\rangle$ is the average acceleration, $\langle L_{min}\rangle$ is the average minimum density gradient scale length, $\langle V_{abl}\rangle$ is the average ablation velocity, and the coefficients α and β are 0.9 and 1.4, respectively. As mentioned in section 2.5, increasing V_{abl} and L_{min} reduces the RTI growth rate and the unstable spectrum exhibits a cutoff around $\approx 90^{26}$. In the case of acceleration phase RTI, the ablative stabilization term can be written as $V_{abl}/V_{imp} \sim \dot{m}_{abl}(I_L)V_{imp}$ and as a consequence[28] the outer surface ablative RTI scales hydroequivalently as long as I_L, α_0 and V_{imp} are kept constant. Instead it has been shown that in the case of the deceleration phase, RTIs don't scale hydroequivalently. In particular, solely because of thermal conduction effects[39],

$$(\frac{V_{abl}}{V_{imp}}) \sim \frac{1}{\sqrt{R}}, \tag{4.9}$$

whereas radiation transport leads to

$$\Big[\frac{(L_{min}/R_h)_{NIF}}{(L_{min}/R_h)_{\Omega}}\Big] \sim 1.5. \tag{4.10}$$

In other words, larger targets exhibit lower ablative stabilization, but see an enhanced stabilization because of density-gradient scale-length. It has been shown[7] that, for single modes, the combination of the effects due to thermal conduction and radiation transport lead to deceleration-phase RTI growth factors that are $\approx 35\%$ higher on NIF than on Omega hydro-equivalent implosions.

Alpha-particle transport is not considered because the hot-spot ignition condition $\chi_{no-\alpha}$ uses no-α parameters. The alpha particles stopped within the hot spot augment the hot spot temperature, and those leaking out of the hot spot deposit their energy at the inner surface of the shell driving mass ablation. As shown in Ref. [33], both mechanisms enhance the ablative stabilization of the RTI. In a NIF size target close to ignition, the stabilization of the RTI from alpha-driven ablation is significant. In the no-α extrapolation of the implosion performance ($\chi_{no-\alpha}$) from OMEGA to NIF, the alpha-driven ablative stabilization is included through the value of the power index μ of the YOC as shown in Eq. (12) of Ref. [12].

It was argued that without ablative stabilization the power index μ would have been larger (≈ 0.8), and (alpha driven) ablativestabilization reduces the power index by half (≈ 0.4). Therefore, the implosion performance metric $\chi_{no-\alpha}$ acquires a correction because of hydrodynamic instabilities given by a factor YOC^{μ} with $\mu = 0.4$:

$$\chi_{no-\alpha} \simeq (\rho R_n)^{0.8}(\frac{T_n}{4.7})^{1.6}YOC^{0.4} \tag{4.11}$$

At this point it's necessary to introduce the main results from the model for alpha heating developed by Betti et al.[3]. This theory allows to estimate the level of alpha heating from the no-α values obtained via hydro-equivalent scaling. This is done by obtaining the value of $\chi_{no-\alpha}$ and $Y_{no-\alpha}$; these two values provide information about the implosion, only accounting for the effects due to compression. Subsequently, the yield including the effect of alpha heating can be obtained using the fitting formula from ref. [3].

The $\chi_{no-\alpha}$ parameter, introduced in equation 4.11, can be expressed in different ways, using different observables. For the purposes of this work, the formulation from refs. [3, 4] is used, namely

$$\chi_{no-\alpha} \approx (\rho R_{no-\alpha})^{0.61}(\frac{0.12Y^{16}_{no-\alpha}}{M^{stag}_{DT}})^{0.34}, \tag{4.12}$$

where "no-α" quantities are the quantities coming from the result of compression alone, $\rho R_{no-\alpha}$ is in g/cm^2, $Y^{16}_{no-\alpha}$ is the yield in units of 10^{16} and M^{stag}_{DT} is the stagnating mass at bang time in mg. While this last term is often approximated as half of the unablated DT mass, for the purposes of the current work the more accurate value coming from the 1-D simulation was used. The choice of the formulation of $\chi_{no-\alpha}$ in equation 4.12 was made because in this form, $\chi_{no-\alpha}$ has a straightforward relation with the ignition criterion ITFx used in connecton to NIF experiments, in particular it is approximately equal to ITFx$^{0.34}$ Assuming $\rho R_{no-\alpha} \sim R, M_{DT} \sim R^3$ and $Y_{no-\alpha} \sim R^{4.3}$ as in equation 4.6, equation 4.12 becomes

$$\chi_{no-\alpha} \sim R^{1.05} \sim E_L^{0.35}. \tag{4.13}$$

Having calculated $\chi_{no-\alpha}$, the yield amplification can be obtained with the following fitting formula from ref. [3]

$$Y_\alpha = \hat{Y}_{amp} Y_{no-\alpha}, \hat{Y}_{amp} \simeq (1 - \frac{\chi_{no-\alpha}}{0.96})^{-0.75}. \tag{4.14}$$

The results from the forementioned theories allowed to obtain theoretical estimates for the hydro-equivalent upscaling of shots 87266 and 88314, with and without the presence of alpha heating. As previously mentioned these were high-adiabat shots, with a large outer diameter. They are the best performing shots obtained on Omega to date and are therefore the best candidates in order to estimate the capabilities of a symmetric direct drive NIF. The theoretical estimates for different laser energies are obtained using the

Table 4.1: Observables for the cores reconstructed in chapter 3. Part I

Shot Number	**Ion Temperature** [keV]	**Hotspot Radius** [μm]	**Areal Density**[mg/cm^2]	
87266, Comp.	4.04	30.0	105	101
88314, Comp.	4.52	25.7	137	133

Table 4.2: Observables for the cores reconstructed in chapter 3. Part II

Shot Number	**Yield** [10^{14}]	**Pressure** [Gbar]	**Burn Width** [ps]	**Bang Time** [ns]
87266, Comp.	1.34	43.5	87	2.151
88314, Comp.	1.31	54.3	70	2.185

data of the reconstructed core, reported in fig.s 4.1 and 4.2 for convenience. The necessary steps have been illustrated in this chapter. From the Omega simulation, the values of $\chi_{no-\alpha}$ are calculated using equation 4.12, and are subsequently scaled to higher laser energies, using equation 4.13. The value obtained is the analytical estimate of the χ_{no_alpha} for the upscaled simulation. The yield on NIF scale is then estimated using equation 4.6. The results of these calculations are shown in table 4.3

It should be mentioned that for the purposes of the current and the following section, the ratios of E_{NIF}/E_Ω are calculated using for E_Ω are the ones actually used in experiment, and not the ones referring to the energy of the pulses used for the 1-D degradation. This was done because the mechanisms that cause the degradation are not known and it is possible for different degradations to lead to the same core. Ultimately, the value of the laser energy that was necessary to obtain implosions 87266 and 88314 was not the laser energy of the pulse used for the reconstruction, but from the original pulse.

The values in table 4.3 were then used to estimate the total yields obtainable on NIF, namely the estimates accounting for alpha heating. The values of the analytical estimates for the yield and the yield amplification are shown

Table 4.3: Neutron yields and values of χ_{no_α}obtained from analytic calculations based on hydrodynamic equivalency, for different laser energies.

Energies	**87266 yield** [10^{16}]	**87266** χ_{no_α}	**88314 yield** [10^{16}]	**88314** χ_{no_α}
1.9 MJ, no alpha deposition	5.58	0.5573	5.48	0.6402
2.0 MJ, no alpha deposition	6.00	0.5674	5.90	0.6518
2.5 MJ, no alpha deposition	8.26	0.6134	8.11	0.7047

Table 4.4: Neutron yields and values of $\hat{Y}_{amp}$ obtained from analytic calculations based on hydrodynamic equivalency, for different laser energies.

Energies	**87266** $\hat{Y}_{amp}$	**87266 yield** [10^{16}]	**88314** $\hat{Y}_{amp}$	**88314 yield** [10^{16}]
1.9 MJ, with alpha deposition	1.92	10.7	2.28	12.5
2.0 MJ, with alpha deposition	1.96	11.7	2.34	13.8
2.5 MJ, with alpha deposition	2.15	17.7	2.70	21.9

in table 4.4. The values in these tables will be compared with the analytic estimates, provided in tables 4.5 and 4.6, in the following section.

4.3 Simulations

In the current section the technique to simulate NIF scale implosions that are hydro-equivalent to the Omega cores reconstructed in chapter **??** is illustrated. This is done in order to validate the theoretical results obtained at the end of 4.2 and in order to obtain accurate estimates of all the quantities characterizing an implosion. The hydrodynamically equivalent scaling, described[28,10] in 4.2, used for the purposes of the current thesis work relies on a very limited number of assumptions, and requires only that the laser instensity, implosion velocity and core pressure are unchanged from OMEGA to NIF scale. These conditions effectively imply that the implosion on the OMEGA laser is replicated on the scale of NIF to reproduce the same energy density (i.e. pressure) over a larger volume, surrounded by a shell of the same density and shape. It should be noted that the above step isn't specific for the Omega and NIF facilities and therefore can be applied to different laser facilities. Only the deceleration phase is simulated, because in ref. [28] it is shown that, if the requirements for hydrodynamically equivalent implosions hold, the acceleration phase of the implosion scales hydro-equivalently.

As mentioned in the introduction, the values considered for E_{NIF} were 1.9, 2.0 and 2.5 MJ; the difference between these is relatively small and, while it significantly affects the yields, the extrapolation technique for 1.9 MJ is no different than that done for the other two energies. Therefore the work done is analogous for all NIF energies (i.e. 1.9, 2.0 and 2.5 MJ). If the conditions for hydro-equivalent scaling hold, the radius and time scale according to[28] equation 4.2; to give an idea of the order of magnitude, (E_{LNIF}/E_{L_Ω}) for the 1.9 MJ case is ≈ 4.08 for both 87266 and 88314.

The process of creating the file containing the input variables from LILAC was similar to the one used in chap 3, with small modifications to the python program provided in appendix A. In particular, it was necessary to multiply all radii in the file by a factor of $(E_{NIF}/E_{\Omega})^{1/3}$, in order to simulate the bigger target. Additionally, in order to obtain all estimates to be compared with the theoretical predictions, in the input deck the following changes were necessary:

- the radius of cutoff was increased by the factor $(E_{NIF}/E_{\Omega})^{1/3}$. While this process appears straightforward, in a few cases it proved necessary to increase the radius of cutoff in order for the simulation to converge. When this proved necessary, the ratio $\frac{r_{cutoff}}{n_{gridpoints}}$ was kept constant and equal to $\frac{r_{cutoff_{\Omega}} * (E_{NIF}/E_{\Omega})^{1/3}}{n_{gridpoints_{\Omega}}}$. In most cases, this step was required for alpha burning simulations; this is because the hot spot pressure amplification due to alpha heating causes a faster disassembly of the target, which is not properly captured by the code; as the core stagnates and begins to expand, the mesh is still imploding, and this leads to the shell "hitting" the numerical boundary (i.e. $r_{cutoff}(t)$) leading either to a crash or to non-physical results.

- account for the presence or absence of alpha heating. All simulations were run with and without alpha heating in order to compare the computational results and the theoretical results from the previous section.

- the duration of the simulation; since in hydro-equivalent implosions time scales as the radius, this value was obtained by multiplying the time chosen for the corresponding OMEGA simulations by $(E_{NIF}/E_{\Omega})^{1/3}$.

As mentioned above, hydrodyamically equivalent scaling causes the two implosions related by hydrodynamic equivalence to have the same pressure. Running simulations with the same amplitudes used for the OMEGA case, it was noticed that the pressure in the NIF simulations didn't match that of the OMEGA simulations by a few Gbar. This suggested that the larger scale affected the linear growth of the perturbation modes introduced. Therefore the upscaled simulations were run with slightly different amplitudes than those in the Omega case, in order to obtain the same inferred pressure for OMEGA and NIF scale. The differences in pressure between the NIF scale simulations were negligible and therefore all three NIF scale implosions have the same mode amplitudes. The changes are the following:

Table 4.5: Neutron yields and values of χ_{no_α}obtained from numerical simulations relying on hydrodynamic equivalency, for different laser energies. The values for the χ_{no_α} in this case are obtained from the observables obtained in the "no-α"simulation, shown in table 4.7.

Energies	**87266 yield** $[10^{16}]$	**87266** χ_{no_α}	**88314 yield** $[10^{16}]$	**88314** χ_{no_α}
1.9 MJ, no alpha deposition	4.46	0.5089	4.60	0.6233
2.0 MJ, no alpha deposition	4.77	0.5262	4.92	0.6332
2.5 MJ, no alpha deposition	6.40	0.6085	6.56	0.6780

Table 4.6: Neutron yields and values of $\hat{Y}_{amp}$ obtained from numerical simulations relying on hydrodynamic equivalency, for different laser energies. It should be noted that in this case, the yield amplification is inferred from the ratio $\frac{\text{yield with alpha deposition}}{\text{yield without alpha deposition}}$.

Energies	**87266** $\hat{Y}_{amp}$	**87266 yield** $[10^{16}]$	**88314** $\hat{Y}_{amp}$	**88314 yield** $[10^{16}]$
1.9 MJ, with alpha deposition	1.77	7.87	1.98	9.10
2.0 MJ, with alpha deposition	1.79	8.56	2.01	9.90
2.5 MJ, with alpha deposition	1.93	12.4	2.22	14.5

- for 87266 it was necessary to increase the amplitude of the mode-2 perturbation used from 2.7% to 3.1%

- for 88314 the ratio of mode 2 to the rest of the spectrum was kept constant, but the amplitude of the mode 2 was decreased from 4.4% to 2.8%. The spectrum used for the NIF scale simulations consisted therefore in a 2.8% mode 2 and a 1.4% flat $+1/l^2$ spectrum. In terms of the variables defined in section 3.4, r and m, r was kept constant, while m was decreased from $m = 2.2$ to $m = 1.4$.

These mode amplitudes allowed to obtain on NIF the same hotspot pressure found for the reconstruction of the Omega implosion.

The yields obtained in the "no-α" case and the values of χ for the upscaled simulations are shown in table 4.5, while the yields in the case of alpha deposition are shown in table 4.6, together with the numerical yield amplification found (i.e. the ratio $\frac{\text{yield with alpha deposition}}{\text{yield without alpha deposition}}$). Comparing these values with the analytical estimates in tables 4.3 and 4.4 it is evident that the numerical simulations provide more conservative estimates for the implosions. Comparing these two sets of tables, namely the ones referring to analytical and numerical estimates, the following conclusions can be drawn, in term of relative errors:

Table 4.7: Results for the 1.9 MJ upscaling of 87266 and 88314 (with and without alpha burning) compared to the reconstructed Ω simulation. Theor. and num. respectively correspond to theoretical and numerical.

Observable	**87266, 1.9 MJ, theor.**	**87266, 1.9 MJ, num.**	**88314, 1.9 MJ, theor.**	**88314, 1.9 MJ, num.**
Ion Temperature [keV]	5.20	4.90	5.82	5.29
Hotspot Radius [μm]	122	119	105	103
Areal Density, MRS	428	414	559	545
Areal Density, ntof	412	403	543	530
Pressure [Gbar]	43.5	42.5	54.3	53.7
Burn Width [ps]	355	338	286	295
Bang Time [ps]	830	846	716	740

- the estimates for the $Y_{no-\alpha}$ are more accurate for 88314 than for 87266 (and all are of the order of 20-30%), while the values of $\hat{Y}_{amp}$ instead follow the opposite trend (all are between 10 and 20 %; this results in estimates of the total Y_α that are overall somewhat more accurate for 87266. This small difference may be simply due to the fact that the values of Y_α are overall higher. It should be noted that the combination of the errors from the $Y_{no-\alpha}$ and from the $\hat{Y}_{amp}$ leads to a higher margin of error in the Y_α, where the relative error varies from 35 to 50 %.

- the $\chi_{no-\alpha}$ is the calculation with the smallest error. In all cases the error is below 10% and for 88314 it is always below 5%.

The values of $\hat{Y}_{amp}$ in table 4.6 are useful for estimating the performance in terms of Q_α. Using fig. 3 in ref. [3], it is possible to infer the values of Q_α: these range from slightly less than 0.5 for the simulation with the smallest $\hat{Y}_{amp}$, corresponding to the 1.9 MJ 87266 simulations, to slightly more than 5 for the case of the highest $\hat{Y}_{amp}$, which is the 2.5 MJ upscaling of 88314.

In an effort to determine if it is possible to attribute these errors to specific observables, in table 4.7, the values of all the upscaled observables for the "no-α" case are shown, compared to the theoretical upscaling from the OMEGA simulations, for the case of 1.9 MJ. Similar considerations can be done for the 2.0 and 2.5 cases. These upscalings rely on the following results from section 4.2: $R, t, \rho R \sim E_L^{1/3}$, the pressure is supposed to be invariant, and the temperatures scale like $\sim E_L^{0.06}$. The results of these simulations are shown in table 4.7, shown together with the analytical extrapolations based on the reconstructions of the Omega implosion: From this table, it is easy to notice that the predicted values are very close to the simulated ones. In particular, all but the time observables are always slightly overestimated, which is most likely the cause for worse results in the predictions of the yields.

The temperature seems to be the observable affected by the biggest error, consisting of 10% for 88314 and roughly 6% for 87266.

Regarding the time observables, it can be seen that apart from the burn width for 87266, which is lower in the simulated case than in the prediction, the time evolution seems to be slightly slower in the simulations than in the predictions. Nevertheless, it is important to note that for such observables the relative errors are very small, all below 5%.

Similar considerations to those above were done for the simulations at 2.0 and 2.5 MJ, giving analogous results.

4.4 Conclusion

In this chapter the analytic scaling first used in ref. [7] is validated using direct simulations and reconstruction of all experimental observables. The OMEGA implosions were first simulated in 1-D using the code LILAC, and compared with experiment. To match the experimental observables, it was necessary to degrade the implosion performance. Both 1- and 2-D mechanisms were used; 1-D degradations consisted in reducing the energy on target with an appropriate modification of the laser pulses, while the 2-D degradations were applied by introducing an appropriate spectrum of nonuniformities at the start of the deceleration phase. The radiation-hydrodynamics code DEC2D was used to simulate the deceleration phase of the implosion starting from the 1-D profiles from LILAC at roughly the time of the end of the laser pulse. In DEC2D, nonuniformities are introduced through angular perturbations of the velocity field on the inner surface of the shell (similar to Ref.[24]) that is RT unstable during the shell deceleration. The spectrum of nonuniformities chosen allowed to obtain a close match with the experimental observables. Different spectrums were used for the two shots analyzed.

Using DEC2D, the simulation was then scaled in size by different factors depending on the chosen NIF laser energies, but identical radial velocity, density, and temperature profiles were kept.Spectra of velocity perturbations similar to the ones found for the Omega simulations were used on the NIF-size simulations. It was found necessary to change the amplitudes of the spectra by small percentages in order to maintain the same inferred pressure.

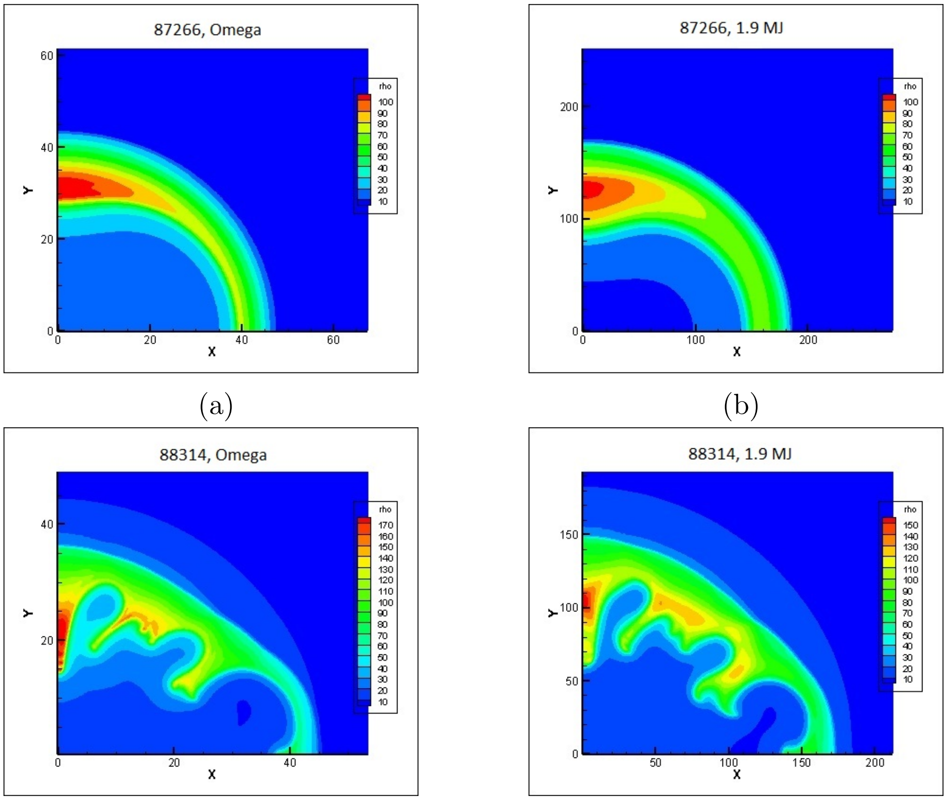

(a) (b)

(c) (d)

Figure 4.1: Mass density profiles at bang time for shots 87266 and 88314, on both Omega and 1.9 MJ NIF scale.

The simulations were performed with and without alpha-energy deposition. Figure 4.1 shows the mass density profiles for the OMEGA simulation and the corresponding 1.9 MJ NIF-scale simulation, for the two shots considered. The shapes are very similar and the only noteworthy difference is the size.

The DEC2D run was then repeated with the alpha-particle energy deposition turned on. The core conditions are shown in table 4.7, compared to their analytically predicted counterparts. Alpha energy deposition produced a yield amplification of up to ≈ 2.2 , reached in the case of the 88314 upscaling to 2.5 MJ, leading to a neutron yield of $\approx 1.5 * 10^{17}$ alphas. Such a yield, would produce an amount of fusion energy of about 410 kJ.

While it was possible to reproduce most of the experimental observables, it should be pointed out that the degradation mechanisms could not be unique; additionally, the causes for the degradation are still uncertain. Neveertheless, this consideration does not affect the results, as the extrapolations are independent of the degradation mechanism affecting OMEGA implosions. Regardless of the degradation mechanism, the hydrodynamic extrapolation to a MJ driver should lead to an approximately unique value of the fusion yield since the alpha heating depends primarily on the no-α Lawson parameter[3].

Chapter 5

Conclusion and Further Work

In this thesis, it was shown that it is possible to reproduce experimental results by degrading the clean implosion using the proper 1- and 2-D degradation mechanisms. Once the implosion core was reconstructed using this method, the simulation was upscaled to NIF conditions using hydrodynamically-equivalent scaling. The results of the upscaling were then compared to the theoretical predictions, relying on ref.s [10, 28]. It was found that when upscaled to 1.9 MJ, which is the highest energy achieved by the NIF laser, would produce a neutron yield of the order of 10^{17} neutrons, or, in terms of total fusion energy produced, would produce more than 250 kJ of energy; this is about 10 times the highest yield achieved on NIF. It was found that with the upscaling of shot 88314, it would be possible to obtain an alpha heating of roughly 2.

As previously mentioned, this study doesn't account for LPIs, hot electrons and other mechanisms that could degrade the performance. It should be mentioned that at bigger scales, the presence of hot electrons could actually be beneficial to the implosion, as long as the hot electrons deposited their energy in the shell; furthermore, with a bigger target, preheating the target wouldn't be as much of a problem as it is on the Omega laser.

The straightforward way to test these predictions would be with a spherically symmetric configuration of laser beams, which NIF is currently not equipped with, and thus would require an upgrade of the NIF facility. It is possible though that some good results could be obtained through the use of polar direct drive (PDD); it is also possible that, limiting cross beam energy transfer (CBET) to the equatorial region, it becomes easier to mitigate. Some experiments on PDD have been done on the Omega facility, and have recently started on the NIF. While the current highest yields obtained are of the order of 10^{12}, it should be kept in mind that these were warm implosions, meaning that the shell is made of plastic, with DD as filler gas, and with a limited mitigation of CBET. These necessary choices significantly affect the obtained yield; the choice of DD alone reduces the yield by almost two orders of magnitude. In order to reach useful goals with PDD it is also necessary to increase the wavelength detuning capability on NIF: it is believed that with a wavelength shift of ±6 Åwould be optimal for CBET mitigation, but NIF currently haas only a capability of 2.3 Å. More experiments for PDD on NIF are currently planned for FY 19 and 20. These are planned both in spherical and in planar geometry, to study the effects of LPIs and CBET mitigation.

There are many possibilities for further work stemming from the current thesis project. The most obvious would be to perform studies of this nature on more and more diverse shots. Different possibilities could be considered:

1. further studies on 87266 and 88314
2. the study of shots similar to 87266 and 88314
3. the study of more diverse shots

Studies of type 1 could provide a more physical basis to the type of 1-D degradation used for the purposes of this thesis. For instance it could be possible that the effect of laser imprinting is not taken properly into account by a 1-D code, and this could lead to more optimistic predictions, therefore it could be interesting to see how important the outer layers of the shell are during the implosion; if neglecting the contribution of the outer shell the implosion remains unchanged, this could be evidence for the small importance of laser imprinting, while if the results were significantly dependent on how much of the shell is neglected, this could support the thesis that imprinting plays a fundamental role in degrading the implosion. A work of this type was already began by the candidate, but was not completed. Many different studies looking into other possible physical mechanisms could be possible.

The goal of studies of type 2 would be useful because it could provide consistency to the results found during this thesis work. This could increase the credibility of such results, providing further support for an upgrade of NIF allowing for spherically symmetric laser illumination, or for smaller investments supporting PDD research: some of these could be an increase in bandwidth for wavelength shifts and cryogenic equipment for direct drive implosions.

Studies of type 3 could prove to be very usedul if they were able to find patterns for different shots; these could give hints as to what are the causes for the degradation of the implosions from the 1-D LILAC predictions. A consistent presence of low modes could be evidence for the effect of the beam stalk, or of the beam port geometry. A presence of mid modes could be explained by imbalances in the laser beams.

Additionally, it could be of use to conduct systematic research on laser pulse shapes for shots already conducted on OMEGA. It is possible that some of them are related by trends similar to those analyzed in section 3.3, and therefore comparisons could be made in order to establish if such changes in the laser pulse have specific advantages.

Lastly, the work done for the purposes of this thesis requires manually running a significant number of simulations, which at times can be based on intuition. Possibly the most efficient way of continuing the work done in this thesis would be to find ways to automate the process, possibly using machine learning algorithms and techniques; this could be important because such an approach may be able to find all the possible mechanisms that can explain the degradation in a given implosion, allowing for a more straightforard and systematic analysis of all shots performed.

Appendices

Appendix A

Deceleration Phase Python Code

In this appendix a description of the Python code used to select the start of the deceleration phase is provided. The purpose of this code is to provide a reasonable choice for the timestep corresponding to the start of the deceleration phase, and, consequently, providing the input deck for DEC2D.

In order to write a code that could be used for various types of shots, it was necessary to rely on very general principles, applicable to all types of shots. The laser pulses can have very different shapes: they can have or not have a foot, they can have one or multiple pickets, and the pickets can be a fraction of the peak power or can even reach the peak power, and be followed by less powerful pulses. The time at which the lasers reaches 2% of the peak power is used as the start time, but it is necessary to find another characteristic time from which to start "tracking" the shock. The length of the laser pulse can go from less than 2 ns to ∼ 4 ns, and these times are often before the bang time, but they can also be after, therefore they're not a good reference time. The only constants in all shots seem to be the presence of a laser, and the presence of a bang time. Therefore the bang time was chosen as the time to start tracking the shock.

Mention that some of the criteria used to consider if a timester was acceptable were Laser Energy, peak neutron production ...

```
#and plots the following, at the time index chosen:
#laser power and total neutron rate in time, with a black
   ↪ bar indicating the time instant chosen
#pressure and density as a function of the radius.
```

```
from lotus import LilacSolution#, LILACInputDeck
import numpy as np
import matplotlib.pyplot as plt
from lotus.utilities.functions import find_nearest

import math

def centered_finite_difference(f, x):
            """
            Simple centered finite difference
            """

            if not isinstance(f, np.ndarray):
                f = np.array(f)

                if not isinstance(x, np.ndarray):
                    x = np.array(x)

            if f.shape != x.shape:
                print("Error in centered_finite_difference:
                   ↪  f and x arrays must be the same
                   ↪ length")
                return None

            dfdx = np.zeros_like(f)
            max_i = len(f) - 1

            # Loop through the internal indices
            for idx in range(1, max_i):
                dfdx[idx] = (f[idx + 1] - f[idx - 1]) / (x[
                   ↪ idx + 1] - x[idx - 1])

            # Fix edges
            dfdx[0] = dfdx[1]
            dfdx[-1] = dfdx[-2]

            return dfdx


plt.close()
```

```
lilac1 = LilacSolution(project_directory='path for folder
    ↪ containing LILAC output')

bang_time = lilac1.ntd.bang_time
bang_time_index = lilac1.ntd.bang_time_index
time_index = bang_time_index


# find the time index when the density gradient and the
    ↪ density maxima start being at the "same" radius, the
    ↪ final time_index
# is the previous time index.

max_density_gradient_index = np.argmax(lilac1.
    ↪ density_gradient[time_index])
max_density_index = lilac1.max_density_index[time_index]
    ↪               #added this preliminary if because I
    ↪ noticed that sometimes
delta_indices = abs(max_density_index-
    ↪ max_density_gradient_index)   # the density and
    ↪ density gradient maxima at bang time are
if delta_indices < 20:
    ↪
    ↪ # too far, so when that is the case I have it do the
    ↪ else option
     while True:
          max_density_gradient_index = np.argmax(lilac1.
              ↪ density_gradient[time_index])
          max_density_index = lilac1.max_density_index[
              ↪ time_index]
          delta_indices = abs(max_density_index-
              ↪ max_density_gradient_index)
          if delta_indices < 25:   #change! before it was 10
               time_index -= 1
          else:
               break
else:
     while True:
          time_index -= 8
          max_density_gradient_index = np.argmax(lilac1.
           ↪ density_gradient[time_index])
        max_density_index = lilac1.max_density_index[
           ↪ time_index]
        delta_indices = abs(max_density_index-
           ↪ max_density_gradient_index)
        if delta_indices < 30:    #here I put 30 because
           ↪ when the two maxima ar far at bang time, they
           ↪  will keep being further than
            time_index -= 1       #for the shots that have
               ↪ the maxima close at bang time
        else:
            break



# now find the local minimum located between the (radial)
   ↪ indices of the maximum density gradient and of the
   ↪ maximum density (-1)
# calculated at time index, and check if it's<0. If it is,
   ↪ check previous time index, and continue until it is
   ↪ not.
# The final chosen time index is the first time index where
   ↪  the forementioned local minimum is negative
# (-1 is necessary because density gradient[time index,
   ↪ radial index[max density]] is not exactly zero, and
   ↪ it may be < or > 0,
# but for the previous index it's pretty consistently a
   ↪ positive value)

max_density_gradient_index = np.argmax(lilac1.
   ↪ density_gradient[time_index])
max_density_index = lilac1.max_density_index[time_index].m

if min(lilac1.density_gradient.m[time_index,min(
   ↪ max_density_gradient_index,max_density_index):max(
   ↪ max_density_gradient_index,max_density_index)])<0:
    while True:
        max_density_gradient_index = np.argmax(lilac1.
           ↪ density_gradient[time_index])
        max_density_index = lilac1.max_density_index.m[
           ↪ time_index]
        density_gradient_local_minimum = min(lilac1.
           ↪ density_gradient.m[time_index,min(
           ↪ max_density_gradient_index,max_density_index)
           ↪ :max(max_density_gradient_index,
           ↪ max_density_index)])
        if density_gradient_local_minimum<0:
            time_index -= 1
        else:
            time_index_chosen = time_index - 3
            break
else:
    time_index_chosen = time_index - 4

if abs(bang_time_index-time_index_chosen)<10:
    time_index_chosen=bang_time_index - 25


maximum_density_index = lilac1.max_density_index[
   ↪ time_index_chosen]
cutoff_radius = lilac1.zonal_radius.m[time_index_chosen,
   ↪ max_density_index]*1.3  # chose 1.3 because 1.5 gave
   ↪ a radius
# that was too close (radial-index-wise) to the first cell
   ↪ with velocity<0 (~few indices, with 1.3 the delta is
   ↪ ~several)

#now find the last radial index for which cutoff radius is
   ↪ > zonal radius [radial index]
radial_index_chosen = find_nearest(lilac1.zonal_radius.m[
   ↪ time_index_chosen], lilac1.zonal_radius.m[
   ↪ time_index_chosen,lilac1.max_density_index[
   ↪ time_index_chosen]]*5/3)[0] - 1


while True:
    if lilac1.zonal_velocity.m[time_index_chosen,
       ↪ radial_index_chosen]>0:
        radial_index_chosen -= 1
    else:
        break


index_perturb = find_nearest(lilac1.density.m[
    ↪ time_index_chosen],lilac1.density.m[time_index_chosen
    ↪ ,lilac1.max_density_index[time_index_chosen]]/math.
    ↪ exp(1))[0]
r_perturb = lilac1.zonal_radius[time_index_chosen,
    ↪ index_perturb].to('um')
fig, (s_plot,t_plot) = plt.subplots (nrows=1,ncols=2,
    ↪ figsize=(30,15))

    # Spatial plot
s_plot.plot(lilac1.zonal_radius[time_index_chosen].to('mm')
    ↪ .m,lilac1.density[time_index_chosen].to('mg/mm^3').m
    ↪ ,'k:',label = 'Mass density')
s_plot2 = s_plot.twinx()
s_plot2.plot(lilac1.zonal_radius[time_index_chosen].to('mm
    ↪ ').m,(lilac1.pressure[time_index_chosen].to('Pa').m)
    ↪ ,'b',label = 'Pressure')
s_plot2.axhline(xmin=0.0,xmax=1.0,y=0.0, linewidth=2, color
    ↪ ='k')
s_plot.set_xlim([0.0,lilac1.zonal_radius[time_index_chosen,
    ↪ radial_index_chosen].to('mm').m])

s_plot.axvline(x=r_perturb.m, ymin=0.0, ymax = 10.0,
    ↪ linewidth=2, color='k')
s_plot2.axhline(xmin=0.0,xmax=1.0,y=0.0, linewidth=2, color
    ↪ ='k')
#s_plot.set_xlim([0.0,0.2])
    # Temporal plot
t_plot2 = t_plot.twinx()
t_plot.plot(lilac1.time.to('s').m,lilac1.laser.power.to('TW
    ↪ ').m,'r')
t_plot2.plot(lilac1.time.to('s').m,lilac1.
    ↪ total_neutron_rate.to('1/s').m,'b')

t_plot.axhline(xmin=0.0,xmax=1.0,y=np.exp(-1)*np.max(lilac1
    ↪ .laser.power.to('TW').m), linewidth=2, color='k')
#t_plot.axhline(xmin=0.0,xmax=1.0,y=7.5)
```

```
t_plot.axvline(x=lilac1.time[time_index_chosen].to('s').m,
    ↪ ymin=0.0, ymax = 1.0, linewidth=2, color='k')
#t_plot.set_xlim(lilac1.time.to('s')[210].m, lilac1.time.to
    ↪ ('s')[250].m)
##this line is to plot the neutron rate



plt.tight_layout()
plt.show()

print('radius of cutoff chosen is')
print(lilac1.zonal_radius.to('um')[time_index_chosen,
    ↪ radial_index_chosen])
print('time chosen is')
print(lilac1.time[time_index_chosen])
print('time index chosen is '+ str(time_index_chosen))
print('radius of perturbation chosen (1 over e) is '+ str(
    ↪ r_perturb))

totals = [lilac1.zonal_radius[time_index_chosen].m*1e4,
    ↪ lilac1.density[time_index_chosen].m,
          lilac1.pressure[time_index_chosen].m, lilac1.
              ↪ zonal_velocity[time_index_chosen].m,
          lilac1.electron_temperature[time_index_chosen].m
              ↪ *1e4, lilac1.ion_temperature[
              ↪ time_index_chosen].m*1e4]

a = np.array(totals)
a1 = np.transpose(a)

np.savetxt('Location to save the file containing the
    ↪ initial conditions for DEC2D', a1, fmt='\%.6G')
```

It should be noted that this code was able to provide acceptable time indices for the start of the deceleration phase for many different types of shots, including but not limited to shots with Germanium doped shells, large ($\sim 500\mu$ m) and small outer diameter shots (~ 1 mm), and more.

Bibliography

[1] Stefano Atzeni and Jürgen Meyer-Ter-Vehn. *The Physics of Inertial Fusion.* Oxfor Science Publications, 2004.

[2] M. M. Basko and J. Meyer-ter-Vehn. "Asymptotic Scaling Laws for Imploding Thin Fluid Shells". In: *Phys. Rev. Lett.* 88 (24 May 2002), p. 244502. DOI: `10.1103/PhysRevLett.88.244502`. URL: `https://link.aps.org/doi/10.1103/PhysRevLett.88.244502`.

[3] R. Betti et al. "Alpha Heating and Burning Plasmas in Inertial Confinement Fusion". In: *Phys. Rev. Lett.* 114 (25 June 2015), p. 255003. DOI: `10.1103/PhysRevLett.114.255003`. URL: `https://link.aps.org/doi/10.1103/PhysRevLett.114.255003`.

[4] R. Betti et al. "Thermonuclear ignition in inertial confinement fusion and comparison with magnetic confinement". In: *Physics of Plasmas* 17.5 (2010), p. 058102. DOI: `10.1063/1.3380857`. eprint: `https://doi.org/10.1063/1.3380857`. URL: `https://doi.org/10.1063/1.3380857`.

[5] H.-S. Bosch and G.M. Hale. "Improved formulas for fusion cross-sections and thermal reactivities". In: *Nuclear Fusion* 32.4 (1992), p. 611. URL: `http://stacks.iop.org/0029-5515/32/i=4/a=I07`.

[6] Arijit Bose et al. "Analysis of Trends in Experimental Observables and Reconstruction of the Implosion Dynamics for Direct-Drive Cryogenic Targets on OMEGA". In: *Submitted to* (2018).

[7] Arijit Bose. *Direct Drive Inertial Con*
nement Fusion: Analysis of the Implosion Core. 2017.

[8] A. Bose et al. "Core conditions for alpha heating attained in direct-drive inertial confinement fusion". In: *Phys. Rev. E* 94 (1 July 2016), p. 011201. DOI: `10.1103/PhysRevE.94.011201`. URL: `https://link.aps.org/doi/10.1103/PhysRevE.94.011201`.

[9] A. Bose et al. "Hydrodynamic scaling of the deceleration-phase Rayleigh–Taylor instability". In: *Physics of Plasmas* 22.7 (2015), p. 072702. DOI: `10.1063/1.4923438`. eprint: `https://doi.org/10.1063/1.4923438`. URL: `https://doi.org/10.1063/1.4923438`.

[10] A. Bose et al. "The physics of long- and intermediate-wavelength asymmetries of the hot spot: Compression hydrodynamics and energetics". In: *Physics of Plasmas* 24.10 (2017), p. 102704. DOI: `10.1063/1.4995250`. eprint: `https://doi.org/10.1063/1.4995250`. URL: `https://doi.org/10.1063/1.4995250`.

[11] Charles Cerjan, Paul T. Springer, and Scott M. Sepke. "Integrated diagnostic analysis of inertial confinement fusion capsule performance". In: *Physics of Plasmas* 20.5 (2013), p. 056319. DOI: `10.1063/1.4802196`. eprint: `https://doi.org/10.1063/1.4802196`. URL: `https://doi.org/10.1063/1.4802196`.

[12] PY. Chang et al. "Generalized Measurable Ignition Criterion for Inertial Confinement Fusion". In: *Phys. Rev. Lett.* 104 (13 Apr. 2010), p. 135002. DOI: `10.1103/PhysRevLett.104.135002`. URL: `https://link.aps.org/doi/10.1103/PhysRevLett.104.135002`.

[13] A. R. Christopherson et al. "A comprehensive alpha-heating model for inertial confinement fusion". In: *Physics of Plasmas* 25.1 (2018), p. 012703. DOI: `10.1063/1.4991405`. eprint: `https://doi.org/10.1063/1.4991405`. URL: `https://doi.org/10.1063/1.4991405`.

[14] J. Delettrez et al. "Effect of laser illumination nonuniformity on the analysis of time-resolved x-ray measurements in uv spherical transport experiments". In: *Phys. Rev. A* 36 (8 Oct. 1987), pp. 3926–3934. DOI: `10.1103/PhysRevA.36.3926`. URL: `https://link.aps.org/doi/10.1103/PhysRevA.36.3926`.

[15] T. Döppner et al. "Demonstration of High Performance in Layered Deuterium-Tritium Capsule Implosions in Uranium Hohlraums at the National Ignition Facility". In: *Phys. Rev. Lett.* 115 (5 July 2015), p. 055001. DOI: `10.1103/PhysRevLett.115.055001`. URL: `https://link.aps.org/doi/10.1103/PhysRevLett.115.055001`.

[16] D. H. Edgell et al. “Mitigation of cross-beam energy transfer in symmetric implosions on OMEGA using wavelength detuning”. In: *Physics of Plasmas* 24.6 (2017), p. 062706. DOI: `10.1063/1.4985315`. eprint: `https://doi.org/10.1063/1.4985315`. URL: `https://doi.org/10.1063/1.4985315`.

[17] M. P. Fewell. “The atomic nuclide with the highest mean binding energy”. In: *American Journal of Physics* 63.7 (1995), pp. 653–658. DOI: `10.1119/1.17828`. eprint: `https://doi.org/10.1119/1.17828`. URL: `https://doi.org/10.1119/1.17828`.

[18] V. N. Goncharov et al. “Improving the hot-spot pressure and demonstrating ignition hydrodynamic equivalence in cryogenic deuterium–tritium implosions on OMEGA”. In: *Physics of Plasmas* 21.5 (2014), p. 056315. DOI: `10.1063/1.4876618`. eprint: `https://doi.org/10.1063/1.4876618`. URL: `https://doi.org/10.1063/1.4876618`.

[19] O. A. Hurricane et al. “Fuel gain exceeding unity in an inertially confined fusion implosion”. In: *Nature* 506 ().

[20] O.A. Hurricane et al. “LLNL-JRNL-648209 (Appendix B)”. In: *Lawrence Livermore National Laboratory* (2014).

[21] I. V. Igumenshchev et al. “Crossed-beam energy transfer in direct-drive implosions”. In: *Physics of Plasmas* 19.5 (2012), p. 056314. DOI: `10.1063/1.4718594`. eprint: `https://doi.org/10.1063/1.4718594`. URL: `https://doi.org/10.1063/1.4718594`.

[22] Thomas B. Kaiser. “Laser ray tracing and power deposition on an unstructured three-dimensional grid”. In: *Phys. Rev. E* 61 (1 Jan. 2000), pp. 895–905. DOI: `10.1103/PhysRevE.61.895`. URL: `https://link.aps.org/doi/10.1103/PhysRevE.61.895`.

[23] P. A. Kharecha and J. E. Hansen. “Prevented mortality and greenhouse gas emissions from historical and projected nuclear power”. In: *Environ. Sci. Technol.* 47 (2013), pp. 4889–4895. DOI: `10.1021/es3051197`.

[24] Roy Kishony and Dov Shvarts. “Ignition condition and gain prediction for perturbed inertial confinement fusion targets”. In: *Physics of Plasmas* 8.11 (2001), pp. 4925–4936. DOI: `10.1063/1.1412009`. eprint: `https://doi.org/10.1063/1.1412009`. URL: `https://doi.org/10.1063/1.1412009`.

[25] A. L. Kritcher et al. “Metrics for long wavelength asymmetries in inertial confinement fusion implosions on the National Ignition Facility”. In: *Physics of Plasmas* 21.4 (2014), p. 042708. DOI: `10.1063/1.4871718`. eprint: `https://doi.org/10.1063/1.4871718`. URL: `https://doi.org/10.1063/1.4871718`.

[26] V. Lobatchev and R. Betti. “Ablative Stabilization of the Deceleration Phase Rayleigh-Taylor Instability”. In: *Phys. Rev. Lett.* 85 (21 Nov. 2000), pp. 4522–4525. DOI: `10.1103/PhysRevLett.85.4522`. URL: `https://link.aps.org/doi/10.1103/PhysRevLett.85.4522`.

[27] Merriam-Webster. *You Can Use ’Whose’ for Things*. URL: `https://www.merriam-webster.com/words-at-play/whose-used-for-inanimate-objects`.

[28] R. Nora et al. “Theory of hydro-equivalent ignition for inertial fusion and its applications to OMEGA and the National Ignition Facility”. In: *Physics of Plasmas* 21.5 (2014), p. 056316. DOI: `10.1063/1.4875331`. eprint: `https://doi.org/10.1063/1.4875331`. URL: `https://doi.org/10.1063/1.4875331`.

[29] John Nuckolls et al. “Laser Compression of Matter to Super-High Densities: Thermonuclear (CTR) Applications”. In: *Nature* ().

[30] P. B. Radha et al. “OMEGA polar-drive target designs”. In: *Physics of Plasmas* 19.8 (2012), p. 082704. DOI: `10.1063/1.4742320`. eprint: `https://doi.org/10.1063/1.4742320`. URL: `https://doi.org/10.1063/1.4742320`.

[31] Richard Rhodes. *The Making of the Atomic Bomb*. 1986.

[32] R.A. Sacks, R.C. Arnold, and G.R. Magelssent. “Irradiation uniformity of spherical heavy-ion-driven ICF targets”. In: *Nuclear Fusion* 22.11 (1982), p. 1421. URL: `http://stacks.iop.org/0029-5515/22/i=11/a=002`.

[33] A. Schiavi and S. Atzeni. “Nonlinear evolution of localized perturbations in the deceleration-phase Rayleigh-Taylor instability of an inertial confinement fusion capsule”. In: *Physics of Plasmas* 14.7 (2007), p. 070701. DOI: `10.1063/1.2751144`. eprint: `https://doi.org/10.1063/1.2751144`. URL: `https://doi.org/10.1063/1.2751144`.

[34] Brian K. Spears et al. “Mode 1 drive asymmetry in inertial confinement fusion implosions on the National Ignition Facility”. In: *Physics of Plasmas* 21.4 (2014), p. 042702. DOI: `10.1063/1.4870390`. eprint: `https://doi.org/10.1063/1.4870390`. URL: `https://doi.org/10.1063/1.4870390`.

[35] Lyman Spitzer Jr. *Physics of Fully Ionized Gases*. 1956.

[36] H. Takabe, L. Montierth, and R. L. Morse. “Self-consistent eigenvalue analysis of Rayleigh–Taylor instability in an ablating plasma”. In: *The Physics of Fluids* 26.8 (1983), pp. 2299–2307. DOI: `10.1063/1.864388`. eprint: `https://aip.scitation.org/doi/pdf/10.1063/1.864388`. URL: `https://aip.scitation.org/doi/abs/10.1063/1.864388`.

[37] H. Takabe et al. “Self-consistent growth rate of the Rayleigh–Taylor instability in an ablatively accelerating plasma”. In: *The Physics of Fluids* 28.12 (1985), pp. 3676–3682. DOI: `10.1063/1.865099`. eprint: `https://aip.scitation.org/doi/pdf/10.1063/1.865099`. URL: `https://aip.scitation.org/doi/abs/10.1063/1.865099`.

[38] Wanguo Zheng et al. “Laser performance of the SG-III laser facility”. In: *High Power Laser Science and Engineering* 4 (2016), e21. DOI: `10.1017/hpl.2016.20`.

[39] C. D. Zhou and R. Betti. “Hydrodynamic relations for direct-drive fast-ignition and conventional inertial confinement fusion implosions”. In: *Physics of Plasmas* 14.7 (2007), p. 072703. DOI: `10.1063/1.2746812`. eprint: `https://doi.org/10.1063/1.2746812`. URL: `https://doi.org/10.1063/1.2746812`.